Title
Light-based tools to dissect spatiotemporal dynamics of Rho GTPase signaling in neutrophils

Permalink
https://escholarship.org/uc/item/2vv945mw

Author
Natwick, Dean

Publication Date
2021

Peer reviewed|Thesis/dissertation

Light-based tools to dissect spatiotemporal dynamics of Rho GTPase signaling in neutrophils

By

DEAN NATWICK
DISSERTATION

Submitted in partial satisfaction of the requirements for the degree of

DOCTOR OF PHILOSOPHY

in

Biochemistry, Molecular, Cellular, and Developmental Biology

in the

OFFICE OF GRADUATE STUDIES

of the

UNIVERSITY OF CALIFORNIA

DAVIS

Approved:

_____
Sean Collins, Chair

_____
Lesilee Rose

_____
Karen Zito

Committee in Charge

2021

i

Acknowledgements

I thank my advisor, Dr. Sean Collins, for being a caring, kind, and patient mentor. What he has taught me, both scientific and otherwise, will serve me well into the future.

I also thank my dissertation committee members, Dr. Lesilee Rose and Dr. Karen Zito. They have been enthusiastic supporters of me, and I am grateful to have had their guidance throughout my PhD.

I also thank my family for their endless love and encouragement.

I especially thank April, who has been through every step of this journey with me. Your selflessness has been unfailing. I truly could not have done it without you.

Abstract

The ability of immune cells to detect, process, and quickly respond to environmental cues is critical for pathogen clearance and mounting inflammatory responses. For instance, neutrophils use chemotaxis- the migration of cells along chemical gradients- to rapidly migrate toward pathogen-derived cues and act as a first line of defense against infection. To do so, neutrophils translate extracellular spatial information into polarized subcellular domains of signaling activity, cytoskeletal rearrangements, and adhesion dynamics. Mounting precise responses to complex inflammatory cues relies upon information processing steps within the chemotaxis signaling cascade. Much of this processing is known to occur through members of the Rho family of GTPases, whose activity is focused by autonomous feedback circuits and crosstalk connections, to activate the necessary signaling pathways at distinct times and subcellular locations. However, limitations in our ability to both measure GTPase activities and perturb signaling inputs with high spatial and temporal resolution have impeded our understanding of neutrophil information processing. In this work, we present new light-based molecular tools and automated imaging assays to simultaneously perturb and measure Rho GTPase activities in space and time. First, we outline a high-resolution chemotaxis assay that allows precise patterning of chemoattractant gradients while simultaneously measuring Rho GTPase activities using FRET-based biosensors. Second, we present an optimized optogenetic strategy for light-based control of protein recruitment to the plasma membrane, which can be used to activate Rho GTPases with precise spatial control. Finally, we pair this optogenetic system with novel red-shifted Rho GTPase FRET biosensors to directly measure crosstalk signaling within the Rho GTPase network. Together, these powerful new tools and experimental approaches provide the capability to dissect information processing by Rho family GTPases with unprecedented spatial and temporal resolution.

Contents

Table of Contents

List of Figures

List of Supplementary Figures

Chapter 1

Introduction

Dean E. Natwick[1]

[1]Department of Microbiology and Molecular Genetics, University of California, Davis, Davis, CA 95616, United States

1.1 Preface

This chapter provides an overview of the relevant background information for the experiments and ideas discussed throughout this work. First, the biological and medical relevance of chemotaxis is discussed. Second, our current understanding of chemotaxis signaling pathways is outlined, with an emphasis on the Rho GTPase polarity circuit. Finally, the advantages and limitations of current molecular tools for understanding spatial Rho GTpase signaling patterns are discussed.

1.2 Chemotaxis: roles in homeostasis and significance in disease

Chemotaxis is the directed migration of cells along chemical gradients. Chemotaxis is seen in diverse biological contexts and underlies many critical cell behaviors. Due to their size, bacteria have evolved a temporal sensing-based mechanism for chemotaxis that allows migration toward nutrient and oxygen sources and away from toxins[1]. Bacterial chemotaxis plays important roles in biofilm formation, quorum sensing, and bacterial pathogenicity, and is being harnessed for bioremediation efforts and emerging drug delivery applications[2]. Eukaryotic cells are larger and capable of spatial gradient sensing during chemotaxis[3]. In multicellular organisms, cells and tissues, such as neural crest cells in vertebrates, exhibit chemotaxis along morphogen gradients to properly pattern the body column during development[4,5]. Axonal growth cones chemotax great distances toward their target sites to ensure proper nervous system wiring[6]. Immune cells also rely upon chemotaxis to migrate through body tissues and fight infections, generate inflammatory responses, and interact with tumors[7]. Thus, defects in chemotaxis are associated with a range of neurological and inflammatory diseases[8–10].

Neutrophils, a type of innate immune cell, have a highly sensitive and accurate chemotactic program that allows them to form one of the first lines of defense against infection[11]. Neutrophils circulate in the blood stream and, upon detection of chemoattractant cues, extravasate through blood vessel walls and migrate through tissues toward infection sites[12]. Once there, they kill pathogens directly via phagocytosis, degranulation, and NETosis, and mediate inflammatory responses of other immune cells locally[12]. A proper balance of neutrophil recruitment is critical for immune function. Defects in neutrophil chemoattraction lead to a host of diseases characterized by susceptibility to frequent infection[13,14]. On the other hand, over-recruitment of neutrophils is a known driver of major inflammatory diseases including chronic obstruction pulmonary disease (COPD), arthritis, and atherosclerosis[7,10,15,16]. In many cases, treatments that specifically target neutrophil recruitment via chemotaxis are lacking[17]. Therefore, understanding neutrophil chemotaxis regulation at a molecular level is necessary for developing more effective and targeted disease treatments.

1.3 Neutrophil chemotaxis signaling programs

Chemotaxis is a complex behavior that requires the integration of spatial chemoattractant gradient sensing with intracellular polarity and motility signaling programs[18]. Though conceptually these three features have distinguishable molecular components and functions, the pathways are tightly interconnected to achieve cell-wide coordination of chemotactic behaviors.

1.3.1 Directional sensing.

Directional sensing refers to the molecular circuits that translate extracellular spatial gradient information into the intracellular signaling activities that guide migration. Chemoattractant sensing is done by G-Protein Coupled Receptors (GPCRs), a vast family of transmembrane receptors capable of detecting diverse chemical cues[7]. Chemoattractant GPCRs couple to heterotrimeric G-Protein complexes containing $G_i\alpha$, $G\beta$, and $G\gamma$ subunits[7,19]. These G-Protein subunits initiate intracellular directionality pathways, which ultimately impinge on cell polarity and motility programs to steer cells[20]. In the unbound state of the GPCR, heterotrimeric G-Protein complexes exist in an inactive state in which the $G_i\alpha$ subunit is bound to GDP. Interaction with an activated receptor causes the $G_i\alpha$ subunit to become GTP-bound, which triggers G-Protein uncoupling from the receptor and dissociation of the trimer into signaling-competent $G_i\alpha$-GTP and $G\beta\gamma$ subunits. Previous work has shown that there is pathway specialization downstream of G-Protein subunits, and that directionality pathways may be controlled specifically by the $G_i\alpha$-GTP subunit[21]. However, the downstream components involved in directional sensing, and how directionality is linked with polarity and motility, are currently unknown.

1.3.2 Cell polarity

During migration, cells generate cell front and rear domains that are defined by polarized morphological and biochemical activities. Polarity signaling is most notably defined by the composition of phosphatidylinositol lipids in the membrane and signaling activities of Rho family GTPases. Front-oriented PI3K activity enriches phosphatidylinositol 3,4,5-triphosphate (PIP3) lipid within the leading-

edge membrane[22,23]. This enrichment is necessary to establish feedback loops that amplify cell front activities[24]. The possible identity and role for a phosphatase that counteracts PI3K activity at the cell rear is ambiguous in neutrophils, though PTEN and SHIP1 have been implicated in this regard[25,26]. Rho family of GTPases have complex, switch-like regulatory patterns to control where and when downstream signaling pathways are active in the cell. The GTPases Rac1, Rac2, and Cdc42 have front-oriented activity patterns and control cell "frontness" pathways, which include branched actin polymerizing activities[27]. Meanwhile, RhoA activity at the rear controls "backness" activities including actomyosin-based contractility[28]. Importantly, the Rho GTPase polarity circuit is "self-generating", as cells will polarize and migrate randomly in the absence of chemoattractant gradients[29]. During chemotaxis, however, Rho GTPases also respond to directional sensing cues within the cell to align the cell polarity axis with the orientation of extracellular gradients for proper steering[30].

1.3.3 Motility

The Rho GTPase polarity circuit feeds directly into the cell motility program. The primary cell motility machinery includes the actin cytoskeleton, adhesion proteins, and their associated regulatory molecules. At the cell front, a branched actin network is polymerized and recycled to generate protrusive forces that propel the leading-edge membrane forward[20]. Meanwhile, actomyosin filaments are generated toward the rear of the cell that create contractile forces that pull the body of the cell along[20]. Importantly, actin polymerization is required for neutrophil motility, as cells treated with latrunculin A, an agent that inhibits actin polymerization, show no morphological polarity or migration[31,32]. In contrast, the role of adhesion complexes in motility is context dependent. In highly confined 3-dimensional environments, neutrophils lacking integrin-based adhesions display normal migration[33]. However, in unconfined 2-dimensional environments, adhesion complexes are essential to gain traction for force generation[33].

1.4 The complexity of the Rho GTPase polarity circuit

Rho GTPases are a family of membrane-associated signaling proteins capable of regulating diverse pathways within the cell. *In vivo*, these GTPases display rapid switch-like signaling behavior.

4

When bound to GDP, GTPases are conformationally inactive. Binding by regulatory proteins called Guanine-nucleotide Exchange Factors (GEFs) promotes release of GDP and exchange for GTP, which switches the GTPase to an activate state[34]. Innate GTP-hydrolysis by Rho GTPases is slow, so these proteins typically remain active until a GTPase-Activating Protein (GAP) binds to initiate GTP hydrolysis and reversion back to an inactive state[34].

One critical feature of Rho GTPases during chemotaxis is their ability to respond to diverse upstream stimuli and to enact different downstream signaling cascades depending on the cellular and environmental context. Much of this capability is conferred through the complex regulatory network of RhoGEFs and RhoGAPs. Neutrophils express roughly 100 RhoGEF and RhoGAP proteins that can respond to different external cues. Additionally, GEFs and GAPs are large, multi-domain proteins with unique modes of localization, activation, and inactivation[35]. These proteins are often incorporated into multi-protein complexes and help to physically link active Rho GTPases with upstream activating cues and appropriate downstream effector proteins[35,36].

The Rho GTPase signaling network is also able to amplify and organize signaling activities into subcellular spatial domains[34]. During chemotaxis, Cdc42 activity is steeply localized toward the cell front. Rac1 activity is also highest at the cell front, though peaks roughly 5 microns behind the leading edge and has a broader activity gradient than Cdc42[30]. Meanwhile, RhoA activity is specifically depleted at the cell front, and is elevated toward the cell body and rear[30]. In this way, the Rho GTPase network acts as a set of signaling hubs that organize different chemotaxis signaling pathways in space and time.

Spatial organization of signaling is largely achieved through non-linear signaling motifs, including crosstalk between Rho GTPase members. Theoretical models have attempted to predict the architecture of Rho GTPase crosstalk patterns based on observed cell behaviors and organizational patterns of known signaling molecules. Additionally, experimental evidence has given insights into some of the details of Rho GTPase crosstalk. In their seminal papers elucidating the roles of Rho GTPases in cytoskeletal regulation, Anne Ridely, Catherine Nobes, and Alan Hall described hierarchical crosstalk from Cdc42 to Rac, and from Rac to RhoA, in fibroblasts[37,38]. Evidence for crosstalk and its roles in

polarity regulation have been demonstrated in immune cell models as well. Using pharmacological

inhibitors and mutants of Rac and RhoA, mutual antagonism between these GTPases was shown to be an

important factor in keeping front and rear signaling domains spatially distinct[28]. More recently, Cdc42-to-

RhoA crosstalk was implicated in macrophage and neutrophil cell lines[30,39]. Ultimately, however, the

temporal kinetics and spatial patterns of Rho GTPase crosstalk have not been directly observed or

measured systematically in neutrophils.

1.5 Challenges in dissecting Rho GTPase signaling during chemotaxis

Resolving Rho GTPase signaling dynamics, especially spatial dynamics, in the context of

chemotaxis has been experimentally challenging. Some tools have been developed that have given some

key insights into this question though. Most notably, live-cell Rho GTPase biosensors, particularly

quantitative FRET-based sensors, have allowed the monitoring of GTPase dynamics in otherwise

unperturbed cells. These sensors have revealed characteristics of Rho GTPase biology including

subcellular spatial patterns and inherent excitability and have given insights into the coupling between

signaling dynamics and cell behavior. Additionally, optogenetic tools, which utilize genetically encoded

light-activated proteins to precisely perturb signaling activities, have recently become important to the

study of Rho GTPases[40]. For instance, light-inducible dimerization tools (LIDs) have been co-opted to

selectively activate single Rho GTPase species in live cells[39,41,42].

Despite these advances, critical limitations remain that have impeded our ability to disentangle

spatial Rho GTPase signaling circuits and how they are integrated with chemoattractant sensing during

chemotaxis. First, though Rho GTPase FRET sensors are widely used, their utilization for studying

subcellular GTPase patterns within stable, well-defined chemical gradients has been challenging. This has

limited our understanding of signal processing from receptors to the polarity and motility machinery.

Second, despite the potential power of optogenetic tools for perturbing GTPase activities with spatial

control, such tools have been under-utilized due to their difficulty of use and poor characterization.

Finally, few tools exist that allow multiplexing of spectrally compatible optogenetic tools and fluorescent biosensors to both perturb and monitor Rho GTPase activities in space and time. This has impeded our ability to dissect features of the Rho GTPase network such as signaling crosstalk, which is a critical part of information processing during chemotaxis.

Throughout this work, tools and approaches that address these specific challenges are presented. In Chapter 2, we present an under-agarose chemotaxis assay that enables high-resolution FRET imaging while patterning defined chemoattractant gradients. In Chapter 3, an optimized LID for subcellular protein recruitment is described. Finally, in Chapter 4, we detail the development of red-shifted Rho GTPase FRET biosensors and their utilization with subcellular optogenetic GTPase perturbation to directly monitor Rho GTPase crosstalk.

1.6 References

(1)   Wadhams, G. H., Armitage, J. P. (2004) Making Sense of It All: Bacterial Chemotaxis. *Nat. Rev. Mol. Cell Biol. 5* (12), 1024–1037. https://doi.org/10.1038/nrm1524.

(2)   Karmakar, R. (2021) State of the Art of Bacterial Chemotaxis. *J. Basic Microbiol. 61* (5), 366–379. https://doi.org/10.1002/jobm.202000661.

(3)   Parent, C. A., Devreotes, P. N. (1999) A Cell's Sense of Direction. *Science 284* (5415), 765–770.

(4)   Kuriyama, S., Mayor, R. (2008) Molecular Analysis of Neural Crest Migration. *Philos. Trans. R. Soc. B Biol. Sci. 363* (1495), 1349–1362. https://doi.org/10.1098/rstb.2007.2252.

(5)   Shellard, A., Mayor, R. (2016) Chemotaxis during Neural Crest Migration. *Semin. Cell Dev. Biol. 55*, 111–118. https://doi.org/10.1016/j.semcdb.2016.01.031.

(6)   Mortimer, D., Fothergill, T., Pujic, Z., Richards, L. J., Goodhill, G. J. (2008) Growth Cone

Chemotaxis. *Trends Neurosci. 31* (2), 90–98. https://doi.org/10.1016/j.tins.2007.11.008.

(7)   Jin, T., Xu, X., Hereld, D. (2008) Chemotaxis, Chemokine Receptors and Human Disease. *Cytokine 44* (1), 1–8. https://doi.org/10.1016/j.cyto.2008.06.017.

(8)   Cartier, L., Hartley, O., Dubois-Dauphin, M., Krause, K. H. (2005) Chemokine Receptors in the Central Nervous System: Role in Brain Inflammation and Neurodegenerative Diseases. *Brain Res. Rev. 48* (1), 16–42. https://doi.org/10.1016/j.brainresrev.2004.07.021.

(9)   Qiu, Y., Zhu, J., Bandi, V., Guntupalli, K. K., Jeffery, P. K. (2007) Bronchial Mucosal Inflammation and Upregulation of CXC Chemoattractants and Receptors in Severe Exacerbations of Asthma. *Thorax 62* (6), 475–482. https://doi.org/10.1136/thx.2006.066670.

(10)   Jasper, A. E., Mciver, W. J., Sapey, E., Walton, G. M. (2019) Understanding the Role of Neutrophils in Chronic Inflammatory Airway Disease. *F1000Research 8* (1), 557.

(11)   Zigmond, S. H. (1977) Ability of Polymorphonuclear Leukocytes to Orient in Gradients of Chemotactic Factors. *J. Cell Biol. 75*, 606–616.

(12)   Kolaczkowska, E., Kubes, P. (2013) Neutrophil Recruitment and Function in Health and Inflammation. *Nat. Rev. Immunol. 13* (3), 159–175. https://doi.org/10.1038/nri3399.

(13)   Lakshman, R., Finn, A. (2001) Neutrophil Disorders and Their Management. *J. Clin. Pathol. 54* (1), 7–19. https://doi.org/10.1136/jcp.54.1.7.

(14)   Aker, M., Zimran, A., Abrahamov, A., Horowitz, M., Matzner, Y. (1993) Abnormal Neutrophil Chemotaxis in Gaucher Disease. *Br. J. Haematol. 83* (2), 187–191. https://doi.org/10.1111/j.1365-2141.1993.tb08270.x.

(15)   Soehnlein, O. (2012) Multiple Roles for Neutrophils in Atherosclerosis. *Circ. Res. 110* (6), 875–888. https://doi.org/10.1161/CIRCRESAHA.111.257535.

(16)   Mazor, R., Shurtz-Swirski, R., Farah, R., Kristal, B., Shapiro, G., Dorlechter, F., Cohen-Mazor, M., Meilin, E., Tamara, S., Sela, S. (2008) Primed Polymorphonuclear Leukocytes Constitute a Possible Link between Inflammation and Oxidative Stress in Hyperlipidemic Patients. *Atherosclerosis 197* (2), 937–943. https://doi.org/10.1016/j.atherosclerosis.2007.08.014.

(17)   Weber, C., Noels, H. (2011) Atherosclerosis: Current Pathogenesis and Therapeutic Options. *Nat. Med. 17* (11), 1410–1422. https://doi.org/10.1038/nm.2538.

(18)   Devreotes, P., Horwitz, A. R. (2015) Signaling Networks That Regulate Cell Migration. *Cold Spring Harb. Perspect. Biol. 7* (8). https://doi.org/10.1101/cshperspect.a005959.

(19)   Metzemaekers, M., Gouwy, M., Proost, P. (2020) Neutrophil Chemoattractant Receptors in Health and Disease: Double-Edged Swords. *Cell. Mol. Immunol. 17* (5), 433–450. https://doi.org/10.1038/s41423-020-0412-0.

(20)   McCann, C. P., Parent, C. A. (2013) Eukaryotic Chemotaxis. *Encycl. Biol. Chem. Second Ed.* 236–240. https://doi.org/10.1016/B978-0-12-378630-2.00421-7.

(21)   Collins, S. R., Yang, H. W., Bonger, K. M., Guignet, E. G., Wandless, T. J., Meyer, T. (2015) Using Light to Shape Chemical Gradients for Parallel and Automated Analysis of Chemotaxis. *Mol. Syst. Biol. 11* (4), 804. https://doi.org/10.15252/msb.20156027.

(22)   Wang, F. (2009) The Signaling Mechanisms Underlying Cell Polarity and Chemotaxis. *Cold Spring Harb. Perspect. Biol. 1* (4), 1–16. https://doi.org/10.1101/cshperspect.a002980.

(23)   Servant, G., Weiner, O. D., Herzmark, P., Balla, T., Sedat, J. W., Bourne, H. R. (2000) Polarization of Chemoattractant Receptor Signaling during Neutrophil Chemotaxis. *Science (80-.). 287* (5455), 1037–1040. https://doi.org/10.1126/science.287.5455.1037.

(24)   Wang, F., Herzmark, P., Weiner, O. D., Srinivasan, S., Servant, G., Bourne, H. R. (2002) Lipid

Products of PI(3)Ks Maintain Persistent Cell Polarity and Directed Motility in Neutrophils. *Nat. Cell Biol.* *4* (7), 513–518. https://doi.org/10.1038/ncb810.

(25) Hannigan, M., Zhan, L., Li, Z., Ai, Y., Wu, D., Huang, C. K. (2002) Neutrophils Lacking Phosphoinositide 3-Kinase γ Show Loss of Directionality during N-Formyl-Met-Leu-Phe-Induced Chemotaxis. *Proc. Natl. Acad. Sci. U. S. A.* *99* (6), 3603–3608. https://doi.org/10.1073/pnas.052010699.

(26) Nishio, M., Watanabe, K. I., Sasaki, J., Taya, C., Takasuga, S., Iizuka, R., Balla, T., Yamazaki, M., Watanabe, H., Itoh, R., Kuroda, S., Horie, Y., Förster, I., Mak, T. W., Yonekawa, H., Penninger, J. M., Kanaho, Y., Suzuki, A., Sasaki, T. (2007) Control of Cell Polarity and Motility by the PtdIns(3,4,5)P3 Phosphatase SHIP1. *Nat. Cell Biol.* *9* (1), 36–44. https://doi.org/10.1038/ncb1515.

(27) Srinivasan, S., Wang, F., Glavas, S., Ott, A., Hofmann, F., Aktories, K., Kalman, D., Bourne, H. R. (2003) Rac and Cdc42 Play Distinct Roles in Regulating PI(3,4,5)P3 and Polarity during Neutrophil Chemotaxis. *J. Cell Biol.* *160* (3), 375–385. https://doi.org/10.1083/jcb.200208179.

(28) Xu, J., Wang, F., Van Keymeulen, A., Herzmark, P., Straight, A., Kelly, K., Takuwa, Y., Sugimoto, N., Mitchison, T., Bourne, H. R. (2003) Divergent Signals and Cytoskeletal Assemblies Regulate Self-Organizing Polarity in Neutrophils. *Cell* *114* (2), 201–214. https://doi.org/10.1016/S0092-8674(03)00555-5.

(29) Wong, K., Pertz, O., Hahn, K., Bourne, H. (2006) Neutrophil Polarization: Spatiotemporal Dynamics of RhoA Activity Support a Self-Organizing Mechanism. *Proc. Natl. Acad. Sci. U. S. A.* *103* (10), 3639–3644. https://doi.org/10.1073/pnas.0600092103.

(30) Yang, H. W., Collins, S. R., Meyer, T. (2016) Locally Excitable Cdc42 Signals Steer Cells during Chemotaxis. *Nat. Cell Biol.* *18* (2), 191–201. https://doi.org/10.1038/ncb3292.

(31)   Coue, M., Brenner, S., Spector, I., Korn, E. (1987) Inhibition of Actin Polymerization by Latrunculin A. *FEBS Lett. 2* (2), 316–318.

(32)   Janetopoulos, C., Ma, L., Devreotes, P. N., Iglesias, P. a. (2004) Chemoattractant-Induced Phosphatidylinositol 3,4,5-Trisphosphate Accumulation Is Spatially Amplified and Adapts, Independent of the Actin Cytoskeleton. *Proc. Natl. Acad. Sci. U. S. A. 101* (24), 8951–8956. https://doi.org/10.1073/pnas.0402152101.

(33)   Lämmermann, T., Bader, B. L., Monkley, S. J., Worbs, T., Wedlich-Söldner, R., Hirsch, K., Keller, M., Förster, R., Critchley, D. R., Fässler, R., Sixt, M. (2008) Rapid Leukocyte Migration by Integrin-Independent Flowing and Squeezing. *Nature 453* (7191), 51–55. https://doi.org/10.1038/nature06887.

(34)   Cherfils, J., Zeghouf, M. (2013) Regulation of Small GTPases by GEFs, GAPs, and GDIs. *Physiol. Rev. 93* (1), 269–309. https://doi.org/10.1152/physrev.00003.2012.

(35)   Hodge, R. G., Ridley, A. J. (2016) Regulating Rho GTPases and Their Regulators. *Nat. Rev. Mol. Cell Biol. 17* (8), 496–510. https://doi.org/10.1038/nrm.2016.67.

(36)   Goedhart, J., van Unen, J. (2019) Molecular Perturbation Strategies to Examine Spatiotemporal Features of Rho GEF and Rho GTPase Activity in Living Cells. *Small GTPases 10* (3), 178–186. https://doi.org/10.1080/21541248.2017.1302551.

(37)   Ridley, A. J., Paterson, H. F., Johnston, C. L., Diekmann, D., Hall, A. (1992) The Small GTP-Binding Protein Rac Regulates Growth Factor-Induced Membrane Ruffling. *Cell 70* (3), 401–410. https://doi.org/10.1016/0092-8674(92)90164-8.

(38)   Nobes, C. D., Hall, A. (1995) Rho, Rac, and Cdc42 GTPases Regulate the Assembly of Multimolecular Focal Complexes Associated with Actin Stress Fibers, Lamellipodia, and Filopodia. *Cell 81* (1), 53–62. https://doi.org/10.1016/0092-8674(95)90370-4.

(39)   O'Neill, P. R., Kalyanaraman, V., Gautam, N. (2016) Subcellular Optogenetic Activation of Cdc42 Controls Local and Distal Signaling to Drive Immune Cell Migration. *Mol. Biol. Cell 27* (9), 1442–1450. https://doi.org/10.1091/mbc.E15-12-0832.

(40)   Tischer, D., Weiner, O. D. (2014) Illuminating Cell Signalling with Optogenetic Tools. *Nat. Rev. Mol. Cell Biol. 15* (8), 551–558. https://doi.org/10.1038/nrm3837.

(41)   Guntas, G., Hallett, R. a., Zimmerman, S. P., Williams, T., Yumerefendi, H., Bear, J. E., Kuhlman, B. (2015) Engineering an Improved Light-Induced Dimer (ILID) for Controlling the Localization and Activity of Signaling Proteins. *Proc. Natl. Acad. Sci. 112* (1), 112–117. https://doi.org/10.1073/pnas.1417910112.

(42)   O'Neill, P. R., Castillo-Badillo, J. A., Meshik, X., Kalyanaraman, V., Melgarejo, K., Gautam, N. (2018) Membrane Flow Drives an Adhesion-Independent Amoeboid Cell Migration Mode. *Dev. Cell 46* (1), 9-22.e4. https://doi.org/10.1016/j.devcel.2018.05.029.

Chapter 2

Parallel high resolution imaging of leukocyte chemotaxis under agarose with Rho family GTPase biosensors

George R. R. Bell[#1], Dean E. Natwick[#1], and Sean R. Collins[*1]

[1]Department of Microbiology and Molecular Genetics, University of California, Davis, Davis, CA 95616, United States

[#] These authors contributed equally.

2.1 Preface

This method was originally published as a chapter in Springer Nature's "Methods in Molecular Biology" book series. A brief overview of the work and its significance to chemotaxis research is provided here.

Bell, G. R. R., Natwick, D. E., Collins, S. R. (2018) Parallel High-Resolution Imaging of Leukocyte Chemotaxis under Agarose with Rho-Family GTPase Biosensors. *Methods Mol. Biol. 1821*, 71–85. https://doi.org/10.1007/978-1-4939-8612-5_6.

2.2 Author contributions

G.R.R.B. and D.E.N. contributed equally to this work. G.R.R.B. and D.E.N. developed the cell culture and under agarose protocols. S.R.C. provided inspiration for the project as well as contributed the image processing sections that detail cell segmentation and alignment as well as ratiometric FRET analysis. G.R.R.B. D.E.N. and S.R.C. contributed to writing the manuscript.

2.3 Abstract

Neutrophils use chemotaxis, the directed migration of cells along chemical gradients, to arrive at sites of infection or inflammation, where they play central roles in clearing pathogens and mediating inflammation[1]. Guidance during chemotaxis requires integrating directional information from chemoattractant receptors with polarity and motility machinery[2,3]. Rho family GTPases are central to this process, though approaches for characterizing Rho GTPase spatial processing during chemotaxis are lacking[4]. To address this, we describe an under-agarose chemotaxis assay that allows high-resolution imaging of neutrophil chemotaxis[5]. The assay is compatible with diverse cell models and imaging modalities. Additionally, we describe how to use UV uncaging of chemoattractants to generate well-defined chemical gradients, and how to measure Rho GTPase activities using FRET-based biosensors. Together, these techniques provide a generalizable, quantitative strategy to measure spatially-patterned Rho GTPase activities within defined environments to better understand information processing during neutrophil chemotaxis.

2.4 Summary of preparation for under-agarose chemotaxis assay

Imaging requires a compound microscope capable of high-resolution FRET imaging, UV irradiation, and must have a heated chamber for live cell imaging. The under-agarose assay is performed on 96-well glass bottom plates, which allows many experimental conditions to be tested in parallel. Prior to the experiment, the glass is treated with a 1% BSA solution and dried completely. The BSA coat allows cells to migrate smoothly along the glass and avoids over-adhesion. On the day of the experiment, a 3% solution of low melting temperature agarose in imaging-compatible media is prepared and allowed to equilibrate to 37 C. A separate solution of imaging-compatible media with caged chemoattractant is prepared and warmed to 37 C. We use N-nitroveratryl-N-formyl-methionine-leucine-phenylalanine (Nv-fMLF) as the caged chemoattractant[6]. Next, cells are prepared at roughly $2x10^5$ cells per milliliter in imaging-compatible media with 10% FBS. Cells are plated by adding a 5 ul drop of cells to the center of

each well of the BSA-treated 96 well plate. After a 5-minute period in which cells settle and adhere to the glass, the agarose and chemoattractant solutions are mixed in a 1:1 ratio and 195 ul of this mixture is very gently pipetted on top of the cell droplet. The mixture should form a uniform, bubble-free layer that confines the cells within a narrow space on the glass (Figure 2.1). The plate is left at room temperature for 30 minutes to allow the agarose to solidify, then the plate is moved to the heated microscope chamber and warmed to 37 C for 30 minutes before imaging.

2.5 Summary of gradient generation using chemoattractant uncaging

UV uncaging of chemoattractant allows for the generation of stable, well-defined chemical gradients. Prior to experiments, the uncaging protocol should be calibrated using caged fluorescein (CMNB-fluorescein), a fluorescent dye that allows direct visualization of the gradient shape over time. Additionally, the strength of the gradient should be calibrated to a suitable magnitude for cell stimulation. This is ideally done by performing UV uncaging experiments with cells loaded with Fluo-3 calcium dye and calibrating the uncaging magnitude such that cells mount a strong calcium response to stimulation. Several different approaches can be utilized for cell stimulation. Most simply, strong, uniform UV irradiation can be performed to generate a uniform chemoattractant stimulus. To generate chemical gradients, the objective Z position can be adjusted prior to UV irradiation, which creates an unfocused light pattern that results in gradient formation. Alternatively, left-to-right or top-to-bottom gradients can be formed by moving the stage X or Y direction prior to UV irradiation and returning to the original field of view for imaging (Figure 2.2). Finally, shorter recharging pulses of UV light every 10 to 60 seconds are often required to maintain gradients over longer time periods.

2.6 Summary of FRET imaging

Imaging cells expressing Rho GTPase FRET biosensors enables cell tracking concomitant with measurement of GTPase activities. During FRET imaging, cells are irradiated with light at the donor fluorophore excitation wavelength and separate images are collected (either simultaneously or in rapid succession) at the donor and acceptor emission wavelengths. Therefore, microscope components must enable irradiation with a narrow excitation wavelength and eliminate bleed-through between emission channels. Stronger light irradiation and faster frame rates give higher signal-to-noise and higher temporal resolution of signaling activities but increase potential for photobleaching. We typically image cells every 3 to 5 seconds for 1 to 5 minutes for chemotaxis experiments. After image collection, proper analysis of FRET image data involves multiple steps of processing that requires a thorough understanding of the corrections needed for your imaging system. Image processing steps typically include careful alignment of donor and FRET images, correction for uneven illumination, background subtraction, and smoothing to reduce pixel noise. Next, cell segmentation is performed to identify cell edges and eliminate non-cell pixels from FRET analysis. Finally, processed and masked images are ratioed on a pixel-by-pixel basis to determine relative FRET activity patterns.

2.7 Concluding remarks

By combining light-controlled chemoattractant stimulation and FRET imaging of Rho GTPase activities in live cells, GTPase signaling dynamics in response to receptor activation and gradient sensing can be measured (Figure 2.3). Understanding how defined spatial gradients are translated into spatiotemporally patterned intracellular signaling activities can give insights into information processing steps within the Rho GTPase signaling network[5]. Furthermore, genetic and chemical perturbations can be used to further dissect the molecular basis for Rho GTPase spatial processing during neutrophil chemotaxis.

2.8 Acknowledgements

2.9 References

(1)   Kolaczkowska, E., Kubes, P. (2013) Neutrophil Recruitment and Function in Health and Inflammation. *Nat. Rev. Immunol. 13* (3), 159–175. https://doi.org/10.1038/nri3399.

(2)   Parent, C. A., Devreotes, P. N. (1999) A Cell's Sense of Direction. *Science 284* (5415), 765–770.

(3)   Devreotes, P., Janetopoulos, C. (2003) Eukaryotic Chemotaxis: Distinctions between Directional Sensing and Polarization. *J. Biol. Chem. 278* (23), 20445–20448. https://doi.org/10.1074/jbc.R300010200.

(4)   Ridley, A. J., Schwartz, M. A., Burridge, K., Firtel, R. A., Ginsberg, M. H., Borisy, G., Parsons, J. T., Horwitz, A. R. (2003) Cell Migration: Integrating Signals from Front to Back. *Science (80-.). 302* (5651), 1704–1709. https://doi.org/10.1126/science.1092053.

(5)   Yang, H. W., Collins, S. R., Meyer, T. (2016) Locally Excitable Cdc42 Signals Steer Cells during Chemotaxis. *Nat. Cell Biol. 18* (2), 191–201. https://doi.org/10.1038/ncb3292.

(6)   Pirrung, M. C., Drabik, S. J., Ahamed, J., Ali, H. (2000) Caged Chemotactic Peptides. *Bioconjug. Chem. 11* (5), 679–681. https://doi.org/10.1021/bc000001g.

2.10 Figures

A
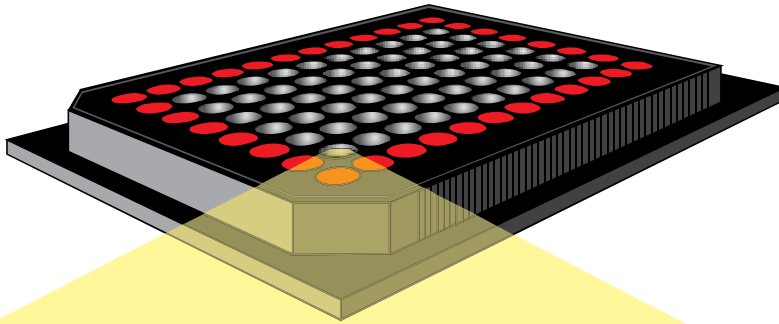
B
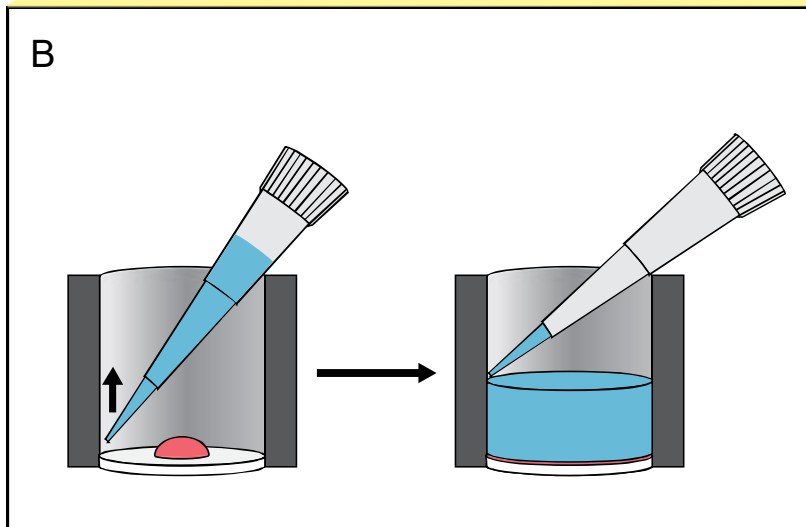
Figure 2.1. Schematic for loading cells under agarose.

(A) A 96-well glass bottom plate for under agarose imaging of chemotaxis is shown. Each well is coated with 1% BSA, washed, and dried prior to the experiment. The wells along the plate periphery are susceptible to temperature fluctuations and should not be used, as indicated by the red highlighting. (B) A diagram of the cell plating and agarose pipetting strategies is shown. A 5 microliter drop of cells (shown in pink) is deposited in the well center and time is given to allow cells to settle on the glass surface. Next, a layer of the liquid agarose-chemoattractant mixture is gently pipetted on top to confine the cells to the well bottom.
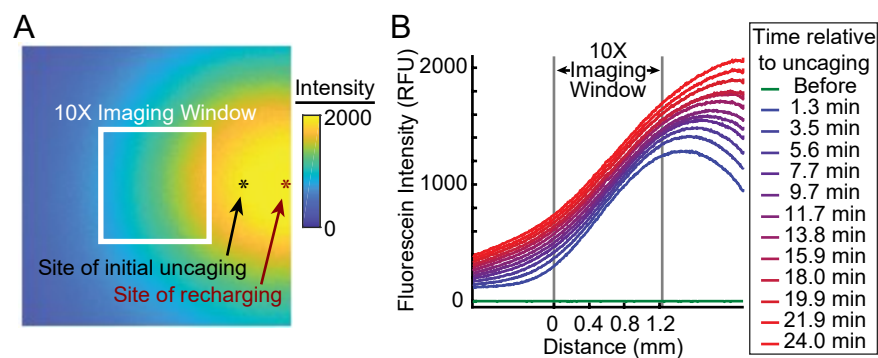
Figure 2.2. Generating stable uncaged chemoattractant gradients.

(A) A chemical gradient is visualized with a 4X objective by uncaging CMNB-fluorescein with UV light at a position shifted in the X direction relative to a 10X imaging window. The gradient is shown after 24 minutes of uncaging. The site of initial uncaging is indicated with a black asterisk, and the site of recharge uncaging is indicated with a red asterisk. The white square indicates the 10X imaging field of view. (B) From the same uncaging protocol as in (A), fluorescein intensity cross sections across the 4X field of view are shown. Vertical lines show the edges of the 10X field of view, and distance in millimeters is indicated along the x-axis.

19
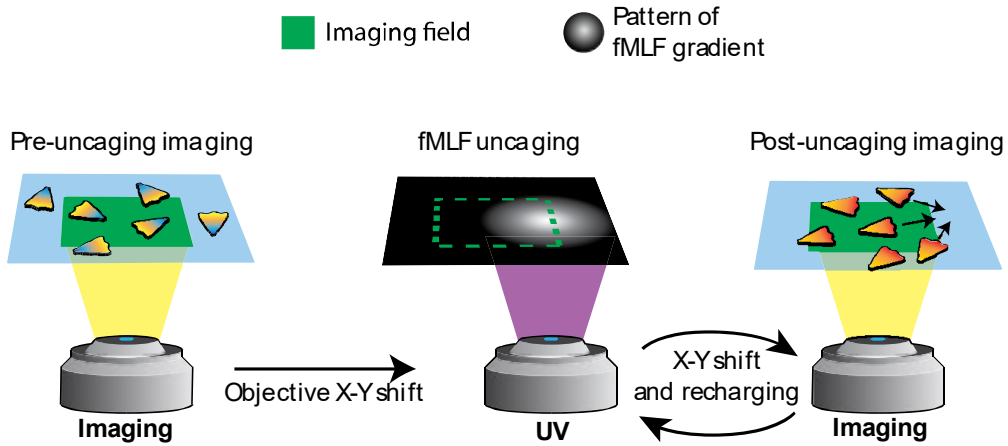
Figure 2.3. Imaging FRET biosensors in cells responding to chemoattractant gradients.

Cells expressing a Rho GTPase FRET sensor are imaged at a starting position prior to chemoattractant uncaging. The microscope stage is shifted in the X or Y direction to generate an off-center gradient, and the stage is shifted back to the original position for post-uncaging imaging. Iterative uncaging and imaging cycles are repeated to monitor migration and Rho GTPase sensor dynamics as cells chemotax over long time periods.

Chapter 3

Optimized iLID membrane anchors for local optogenetic protein recruitment

Dean E. Natwick[1] and Sean R. Collins[1]*.

[1]Department of Microbiology and Molecular Genetics, University of California, Davis, Davis, CA 95616, United States

3.1 Preface

This chapter describes novel optogenetic constructs with reduced diffusion coefficients and optimized expression levels for strong, highly localized protein recruitment to the plasma membrane to study subcellular signaling activities. This work was originally published as a research article in *ACS Synthetic Biology*.

3.2 Author Contributions

D.E.N. and S.R.C. conceived and designed the experiments. D.E.N. generated all constructs and cell lines, and performed all experiments and data analyses. S.R.C. wrote the mathematical models and oversaw their application by D.E.N. D.E.N. wrote the manuscript with input from S.R.C. and acknowledged colleagues.

3.3 Introduction

To execute fundamental processes including division, migration, and cell-to-cell communication, cells use signaling networks to organize protein activities within subcellular regions [1–5]. Non-linear network topologies that include fast-acting feedback and crosstalk connections shape the outputs of these networks in space and time [6,7]. However, identifying these motifs and understanding their roles have been pervasive challenges in cell biology. Recently, optogenetic tools have provided new opportunities to dissect complex signaling mechanisms by permitting specific activation of a single protein species at precise times and subcellular locations [8–12]. In this way, signaling motifs can be directly probed to understand the roles of individual components and how they fit together to control complex cell behaviors.

The plasma membrane is a primary scaffold upon which signaling networks are organized [13]. Indeed, concentrating upstream regulatory proteins, enzymes, and downstream effectors in distinct locations at the plasma membrane is a critical way to connect ligand sensing with localized signaling outputs. For instance, activated G-protein coupled receptors trigger asymmetric recruitment of lipid modifying enzymes and Rho GTPase regulators to polarize cells during migration [14–16]. Receptor tyrosine kinases similarly recruit SH2 domain-containing proteins to distinct membrane locations to initiate diverse adhesive, metabolic, and proliferative signaling programs [17]. Further downstream, actin regulating proteins are commonly recruited and concentrated at localized sites on the membrane to give cells shape, build specialized structures, or generate forces for movement [18,19]. Engineering exogenous regulation of protein localization and activation at the plasma membrane represents an important step in dissecting, and ultimately controlling, diverse cell behaviors.

Optogenetic light-inducible dimer systems are especially valuable tools for rapid recruitment of specific proteins to the plasma membrane to study their effects with high spatial resolution. Several systems have been developed from naturally occurring photosensory protein families including phytochromes, cryptochromes, and light-oxygen-voltage (LOV) domain proteins [9–12]. These domains vary in size, activation mechanism, and absorption wavelength to confer different properties to each system [20]. Among

the optogenetic systems, the improved Light-Induced Dimer (iLID) system has emerged as a leading tool because of its ease of use, fast kinetics, and large fold-change in component protein association [12]. iLID is an engineered protein composed of a blue-light-sensing LOV2 domain and a flanking C-terminal helix (termed the Jα helix) fused to seven residues from the *E. coli* SsrA peptide that can bind with high affinity to the *E. coli* adaptor protein SspB [17]. In iLID's dark state conformation, tight "docking" of the Jα helix to the LOV core sterically prohibits SsrA-SspB interaction. However, upon irradiation with blue light, conformational changes in the LOV domain lead to helix undocking and heterodimerization between iLID and SspB. Dimerization occurs within seconds and persists until iLID reverts to its dark state. The dimer half-life (~30 seconds) is shorter than most other optogenetic tools, but it can still limit temporal experimental control. By anchoring iLID to the inner leaflet of the plasma membrane and fusing SspB to protein domains of interest, the system has been used to selectively activate Rho GTPases for migration, modulate Erk signaling during *Drosophila* development, and generate pulling forces for mitotic spindle positioning [21-23].

For maximum control of protein localization, an ideal light-inducible dimer system should display minimal interaction in the dark, a large fold-change in recruitment, and exact localization to the stimulated region for appropriate timescales. In practice, however, precision is limited by the physical properties of cells and biomolecules, including protein expression and diffusion. Due to non-negligible dark state binding and laws of mass action kinetics, the SspB component of the iLID system shows basal membrane localization that scales with protein levels [24]. As a result, relative expression levels must be considered to strike a fine balance between basal and light-induced recruitment. Variability in expression on a cell-by-cell or construct-dependent basis exacerbates this issue, negatively impacting biological reproducibility and consistency across research groups [25]. Additionally, lateral diffusion of the iLID component in the membrane limits spatial control for recruitment, especially for applications that require subcellular localization for extended periods of time [26]. iLID is typically targeted to the membrane via fusion to the C-terminal CAAX motif of KRAS, which includes a post-translational prenylation site [27]. This small lipid anchor could permit diffusion at a rate of ~0.5-1.7 mm^2/sec, meaning that an activated iLID molecule may

diffuse roughly 7 mm away from its site of activation before reverting to its dark state [28,29]. For many cell types with diameters in the 20-30 mm range, the resulting recruitment zone would extend across a large proportion of the cell area. Ultimately, these sources of noise and variability pose major limitations to optogenetic dimerization systems including iLID that have not been collectively addressed.

To alleviate these challenges, we generated iLID proteins with membrane anchors of different sizes and fusion configurations, and we systematically compared their subcellular recruitment dynamics using quantitative imaging. We showed that N-terminal anchoring configurations allow stronger recruitment compared to the existing C-terminal version, and that larger membrane anchors display slower diffusion and greatly improved spatial confinement of recruited proteins. We used mathematical modeling to define optogenetic component expression regimes to achieve optimal recruitment with different iLID fusions across diverse applications. Furthermore, we demonstrated that our slow-diffusing iLID proteins exhibit stronger local recruitment over wider component expression ranges.

3.4 Results

3.4.1 A diverse set of membrane-anchored iLID fusion proteins

We theorized that the C-terminal CAAX motif that is typically used to anchor iLID to the plasma membrane may influence subcellular recruitment dynamics (Figure 1A). First, the anchor's proximity to the SsrA peptide could negatively affect iLID's binding availability in the lit state. Second, the anchor's small size and large diffusion coefficient contribute to the rapid spread of activated iLID molecules away from sites of stimulation, leading to poor spatial confinement of recruited proteins over time. To address these issues, we designed three alternative iLID fusion proteins that we hypothesized would show stronger recruitment and tighter localization (Figure 1B). To test the consequences of relocating the lipid anchor away from the SsrA peptide, we fused 11 residues from Lyn kinase, which contain post-translational myristoylation and palmitoylation sites, to the N-terminus of iLID (Lyn11-iLID) [30]. Additionally, to compare protein confinement when iLID is anchored with slow-diffusing protein

domains, we fused either the four-pass transmembrane protein Stargazin or the seven-pass transmembrane protein ADRB2 to the N-terminus of iLID (Stargazin-iLID and ADBR2-iLID, respectively) [31,32]. Notably, another group previously used Stargazin to localize another optogenetic construct, LOVpep, to the membrane, and recently used it to anchor iLID to the membrane in *Drosophila* [33,34]. We also fused mTurquoise2 directly upstream of iLID in all constructs to allow imaging of iLID expression and localization concurrent with activation using a 445 nm laser (Figure 1C). Each construct was stably expressed in HEK-293T cells, and imaging by confocal microscopy confirmed that all iLID constructs were sharply localized to the plasma membrane, although ADRB2-iLID fluorescence was noticeably dimmer than the other constructs (Figure 1D).

3.4.2 N-terminal membrane anchors allow stronger recruitment

To assess recruitment magnitude and diffusive spread of the different iLID fusion proteins, we developed an automated point-recruitment assay using total internal reflection fluorescence (TIRF) microscopy. In TIRF microscopy, an induced evanescent field illuminates fluorophores exclusively within a ~100-200 nm thin region adjacent to the cell-glass interface. This imaging modality allowed us to monitor recruitment and diffusion of SspB molecules at the membrane while visualizing only a small fraction of background cytosolic protein (Supplemental Figure S1). We stably co-expressed each iLID construct with SspB fluorescently tagged with tandem dimer Tomato (tdTom-SspB) in HEK-293T cells. We monitored point-recruitment by performing TIRF imaging of tdTom-SspB every second for 25 seconds, with a single 10 ms pulse of 445 nm light applied within a ~3 mm radius spot at the cell centroid between frames 5 and 6 (Figure 2A). Importantly, we wrote a custom script to automate these experiments to reduce bias in cell selection, improve experimental reproducibility, and increase the number of biological replicates. To quantify recruitment magnitude, we calculated the fold change in SspB signal at the stimulus site by normalizing SspB values to the pre-stimulus level in each cell and calculating the mean time course over all cells. Intriguingly, Lyn11-iLID and Stargazin-iLID showed markedly higher recruitment compared to iLID-CAAX, while ADRB2-iLID showed slightly reduced recruitment (Figure 2B). Furthermore, non-

normalized SspB intensity before stimulation was similar for all conditions, though perhaps slightly elevated for Lyn11-iLID compared to other constructs. This suggested that differences in recruitment were primarily due to changes in binding interactions in iLID's lit state (Figure 2C). It should be noted, however, that the non-normalized measurements depend on the degree of basal binding as well as total iLID and SspB protein levels in each cell. Therefore, we could not definitively assess possible differences in dark state binding between the iLID fusion proteins.

Disparities in iLID expression levels between the constructs could account for the differences in SspB recruitment that we found. To investigate this possibility, we assessed relative iLID protein concentration at the membrane using fluorescence intensity from iLID TIRF images. We found that average fluorescence was highest for iLID-CAAX and Lyn11-iLID, ~33% lower for Stargazin-iLID, and ~75% lower for ADRB2-iLID (Figure 2D). Therefore, our alternative iLID fusion proteins show improved recruitment despite similar or lower expression levels. Notably, iLID-CAAX and Lyn11-iLID had roughly equivalent expression levels and differed only in the location of the lipid anchor, suggesting that the N-terminal location of the anchor is crucial for strong recruitment. Indeed, when we used global illumination for cell-wide recruitment and analyzed cells with matched iLID expression levels, we found that the Lyn11 and Stargazin anchors gave markedly stronger recruitment than the CAAX anchor (Supplemental Figure S2). In the case of ADRB2-iLID, drastically lower expression likely outweighs the potential improvements from N-terminal anchoring and results in a net reduction in SspB recruitment.

We observed considerable variability in iLID fluorescence at the single cell level, which we hypothesized could drive heterogeneity in SspB recruitment (Supplemental Figure S3). Indeed, when we plotted the maximum fold change in SspB signal against iLID fluorescence in individual cells, we found a positive correlation for all constructs, supporting that higher iLID concentrations allow more SspB to be brought to the membrane upon stimulation (Figure 2E-H). Consistent with our global illumination experiments, the slope of this correlation was larger for the N-terminally anchored iLID fusion proteins compared to iLID-CAAX. In contrast, however, the slope of the correlation also increased corresponding to anchor size, suggesting that slow diffusion also contributes to higher local recruitment (Supplemental

Figure S4). Taken together, our results demonstrate that localizing iLID to the membrane with a slow-diffusing N-terminal anchor enables stronger recruitment of SspB, even at lower iLID concentrations, and that this is achieved in large part through improved iLID-SspB interactions in the lit state.

3.4.3 Mathematical models for guided optimization of iLID-based membrane recruitment

Since our point-recruitment assay results indicated that component expression has a major impact on recruitment efficiency, we developed differential equation models to define iLID and SspB expression regimes for optimal system performance. We modeled the iLID system as a reaction-diffusion system with four possible binding/activation states. Prior to stimulation, the system exists in a dynamic equilibrium between two states. In the first state, iLID molecules are inactive and unbound (free $iLID_{dark}$) and SspB molecules are cytoplasmic (free SspB) (Figure 3A, top left). In the second state, SspB molecules are bound to inactive iLID at the membrane to form $iLID_{dark}$-SspB dimers, which represents basal SspB recruitment (Figure 3A, bottom left). Upon light stimulation, iLID is rapidly converted to its active state, where it can then exchange between unbound (free $iLID_{lit}$, free SspB) and bound ($iLID_{lit}$-SspB) states (Figure 3A, top-right, bottom-right). We assumed that activation and dark-state reversion of iLID occur independently of its binding state, with activation depending on the light intensity, light duration, and the iLID activation rate, and reversion depending on the intrinsic rate of iLID relaxation. Importantly, we were able to use previously reported measurements for iLID-SspB binding affinities in the lit (0.13 mM) and dark (4.7 mM) states and estimates of the iLID dark-state reversion rate ($\sim$0.02 s^{-1}) to limit the number of free parameters in the model. Additionally, for modeling subcellular recruitment, we modeled the diffusion of all iLID-containing complexes with a single diffusion coefficient. We used the model to simulate the concentrations of its five molecular species (free $iLID_{dark}$, free $iLID_{lit}$, $iLID_{dark}$-SspB, $iLID_{lit}$-SspB, and free SspB) over the course of prototypical light-stimulation experiments.

3.4.4 An optimal expression regime for cell-wide recruitment

Since iLID is often used to recruit proteins uniformly to the entire plasma membrane, we reasoned that global recruitment experiments provided both an ideal simplified system for validating our model, and

a highly relevant system for optimizing component expression levels. Therefore, we first used an ordinary differential equation (ODE) version of our model lacking the diffusion terms to predict basal recruitment, maximum absolute recruitment, fold enrichment, and dissociation half-time upon cell-wide iLID activation (Figure 3B-3C). Note that, because TIRF measurements include signal from a small fraction of cytoplasmic protein (Supplemental Figure S1), empirical measurements of fold recruitment will differ from the predicted fold enrichment values, particularly for low iLID concentrations. We ran our model for a range of iLID-to-SspB ratios, titrating each component concentration between 10 nM and 10 mM to encompass the iLID-SspB affinity range for iLID dark and lit states.

As expected, both basal and max recruitment scaled with protein levels. At low iLID and SspB concentrations, our model showed minimal basal recruitment but weak absolute recruitment. In contrast, high iLID and SspB concentrations yielded high basal recruitment and strong absolute recruitment (Figure 3D-E). Because basal and absolute recruitment were correlated but with shifted dose-response curves, low component concentrations gave larger fold-changes in SspB recruitment (Figure 3F). Therefore, fold enrichment and absolute recruitment were largely inversely correlated. Notably, for a given level of basal recruitment, the maximum fold enrichment always occurred when iLID and SspB protein levels were equal (Figure 3F). Thus, for global recruitment strategies, equal expression of the two components is ideal, although the optimal levels will depend on a compromise between basal and stimulus-induced recruitment.

Interestingly, the model also made a less intuitive prediction: the time for iLID-SspB dissociation will be longer when iLID concentrations are high and in excess over SspB (Figure 3G). This effect is due to the increased likelihood of SspB re-binding to a neighboring molecule when more iLID is present at the membrane. We set out to test this prediction to validate our model, and to determine whether this effect occurs in the range of expression levels achieved in our cell lines. Using time lapse confocal microscopy, we measured the depletion and recovery of SspB signal in the cytoplasm before and after global iLID stimulation (Figure 3H). We observed characteristic rapid depletion and then gradual recovery of cytoplasmic signal, though the magnitude and kinetics varied from cell to cell (Supplemental Figure S5). We organized the single cell data into four groups based on estimated iLID-to-SspB ratio and plotted curves

for each group adjusted to a 0 to 1 scale to facilitate temporal comparisons. We used pre-stimulation SspB fluorescence as a measure of relative SspB concentration. Because iLID fluorescence in individual cells could not be measured directly in our assay, we used maximum percent signal loss to infer relative iLID concentrations, as iLID concentration and fold recruitment were strongly correlated in our previous experiments. In agreement with the model prediction, groups with higher estimated iLID-to-SspB ratios showed slower recovery of SspB signal and had recovery curves that qualitatively matched curves generated using our model (Figure 3I-3J).

Given the above findings, we suggest guidelines for component expression in optogenetic experiments using global recruitment. Low component concentrations are preferable when fast kinetics are important and only low levels of SspB recruitment are necessary. For applications requiring higher levels of SspB recruitment, intermediate component concentrations are optimal, as very high concentrations may suffer from high basal binding and poor enrichment. In both cases, the two component concentrations should be matched as closely as possible to best balance basal and absolute recruitment.

3.4.5 An optimal expression regime for subcellular recruitment

The requirements for effective local recruitment can differ markedly from those for cell-wide recruitment. For instance, limitations on recruitment magnitude and kinetics may be altered since fewer component proteins participate, and the effect of diffusion becomes a major consideration. We therefore used a partial differential equation (PDE) model to assess optimal expression regimes for subcellular recruitment and investigate the effects of anchor diffusion (Figure 4A). As with our ODE model, we titrated iLID and SspB concentrations between 10 nM and 10 mM and calculated the expected fold enrichment by recruitment. We began by using an iLID diffusion coefficient of 1 mm^2/sec as an estimate for the diffusion of iLID-CAAX, which falls within the range of measured diffusion rates for similar proteins [28,29]. Distinct from our ODE model prediction, we found that optimal fold enrichment was achieved with iLID concentrations in excess of SspB by roughly 4-fold (Figure 4B). This arises because basal recruitment was similar to our ODE model predictions, while max absolute recruitment was high at lower SspB

concentrations relative to iLID (Supplemental Figure S6A, S6C). From these observations, we hypothesized that cells with high SspB concentrations would show lower fold recruitment on our point-recruitment assay. To investigate this, we overlaid single cell pre-stimulation SspB fluorescence values onto the correlation plots from Figure 2E-2H and looked for trends in recruitment according to basal SspB concentrations. It was important to compare only cells within conditions at similar iLID levels since pre-stimulation SspB fluorescence could also be affected by basal binding to the iLID components. Consistent with our expectations, we found that, at a given iLID concentration, cells with high SspB levels tended to have lower fold recruitment while cells with low SspB levels had higher fold recruitment (Supplemental Figure S7).

Next, we asked whether the iLID diffusion coefficient affects the optimal component concentration regime. For comparison, we adjusted the iLID diffusion coefficient to 0.1 mm^2/sec, an estimate for Stargazin-iLID based on diffusion rates of other transmembrane proteins [35]. Intriguingly, we found that optimal recruitment was achieved with an even stronger asymmetry in concentrations, with up to almost 10-fold excess of iLID over SspB (Figure 4C). Again, this was due to high max absolute recruitment at even lower SspB concentrations (Supplemental Figure S6B, S6D). We hypothesized that, with slower diffusion, iLID molecules are better retained at the stimulation spot as maximum recruitment is being achieved, allowing higher absolute recruitment at low SspB levels. This would cause lower recruitment for fast-diffusing proteins compared to slow-diffusing proteins. To test this, we plotted the expected absolute recruitment for systems with diffusion coefficients of 1 or 0.1 mm^2/sec. Across a range of iLID concentrations, modeled recruitment was higher with the slower diffusion coefficient (Figure 4D). Importantly, this finding provides a possible explanation for our previous observation that the slopes of the correlations between iLID fluorescence and recruitment increased with anchor size (Supplemental Figure S4).

Another prediction of our model is that the time to maximum recruitment (t_{max}) depends on the membrane anchor diffusion and the relative component concentrations. We calculated t_{max} values at different iLID-to-SspB ratios with diffusion coefficients of 1 mm^2/sec or 0.1 mm^2/sec. Our model generally

predicted higher t_{max} values with the slow-diffusing anchor (Figure 4E-4F). Interestingly, we also observed that t_{max} was markedly higher when iLID was in strong excess over SspB. This effect arises because iLID can deplete free SspB locally, and further recruitment depends on long-range SspB diffusion. To determine whether this behavior was evident in our point-recruitment experiments, we took cells with a narrow range of SspB fluorescence values, grouped them based on iLID fluorescence, and plotted average recruitment curves. For both iLID-CAAX and Stargazin-iLID cells, we observed the predicted shift in t_{max} values, and Stargazin-iLID showed shifted t_{max} values and higher recruitment magnitudes at lower iLID levels (Figure 4G-4H).

Ultimately, the iLID and SspB expression ranges for optimal subcellular recruitment depend on the nature of the iLID membrane anchor and the experimental goals. To explore this in more detail, we set out to characterize the conditions for optimal recruitment with both fast and slow diffusing anchors, given a set of desired system constraints. As a model case, we defined optimal recruitment as having no more than 50 nM basal recruitment, at least 100 nM max absolute recruitment, and at least a 10-fold increase in recruitment after stimulation. We then plotted contour lines for these three features and shaded the region in which all criteria were met. With fast diffusion, optimal recruitment was achieved within a relatively narrow range of expression levels (iLID concentrations between ~300 – 900 nM and SspB concentrations between ~75 – 250 nM) (Figure 4I). With slow diffusion, however, the range of iLID and SspB expression values for optimal recruitment was markedly wider, encompassing both higher and lower expression levels for each component (iLID concentrations between ~200 nM – 5 uM and SspB concentration between ~30 – 600 nM) (Figure 4J). This illustrates that experiments using slow-diffusing versions of iLID can better tolerate heterogeneity in expression levels, which is another key benefit to our alternative iLID fusions.

3.4.6 Larger iLID anchors improve spatial confinement of recruitment

Our primary goal in building iLID membrane anchors with slower diffusion was to improve the spatial confinement of recruited proteins over time. To test whether this indeed occurred, we used the data from our point-recruitment assay to generate spatial SspB intensity gradients at each time point after

stimulation. After normalizing SspB values to pre-stimulation levels, we measured the mean intensity as a function of radial distance from the stimulation site. Consistent with our expectations, we found that larger iLID anchor sizes resulted in improved confinement of SspB signal with sharper boundaries. As expected, the spatial extent of the initial SspB gradients right after stimulation was very similar for all iLID fusion proteins, despite differences in recruitment magnitude (Figure 5A-5D, dark green curves). However, at longer times after stimulation, SspB gradients spread and flattened to different extents that corresponded to the diffusion properties of the iLID membrane anchors. Signal spreading was most pronounced with iLID-CAAX and was slightly improved with Lyn11-iLID, likely owing to the presence of an additional post-translational lipidation site (Figure 5A-5B, yellow curves, and Supplemental Movie S1, S2). However, it was markedly improved for Stargazin-iLID and ADRB2-iLID (Figure 5C-5D, yellow curves, and Supplemental Movie S3, S4). Indeed, when we used the distance for half-maximal gradient signal as a measure of spatial spread, we observed that between 1 and 10 seconds post-stimulation, the spread increased 65% for iLID-CAAX and 55% for Lyn11-iLID, but only 21% for Stargazin-iLID and 19% for ADRB2-iLID (Figure 5E).

To confirm that the observed differences in SspB signal spread were due to diffusion, we performed fluorescence recovery after photobleaching (FRAP) experiments using confocal microscopy. Using a focal plane through the middle of the cell, we photobleached a 5 mm region of the membrane and measured the rate of fluorescence recovery, which serves as a direct measure of iLID-anchor mobility (Supplemental Figure S8). These experiments were performed in cells without the SspB construct to ensure that SspB binding would not alter apparent diffusion rates. Consistent with our TIRF experiments, we found that recovery was fastest with iLID-CAAX, slower with Lyn11-iLID, and markedly slower for Stargazin-iLID and ADRB2-iLID (Supplemental Figure S8). We fit diffusion coefficients of 0.85, 0.4, 0.1, and 0.1 mm^2/sec for the CAAX, Lyn11, Stargazin, and ADRB2 constructs, respectively (Supplemental Figure S8). The calculated diffusion coefficients for iLID-CAAX and Stargazin-iLID agree with our predictions and suggest that the diffusion coefficients we used in our model encompass an appropriate range.

Slow iLID diffusion is especially important to improve spatial confinement of recruitment over longer timescales. To more clearly demonstrate this, we performed a longer multi-stimulation recruitment experiment in which we repeatedly stimulated iLID every 10 seconds with a 10 ms light pulse over a 1-minute period. We then compared initial and final SspB gradients. Because Stargazin-iLID stood out as our best performing iLID fusion protein for subcellular recruitment, we focused our comparison on iLID-CAAX and Stargazin-iLID. With iLID-CAAX, the SspB gradient was initially localized, though relatively small in magnitude. Over time, the gradient spread and flattened drastically, showing elevated signal as far as 20 mm from the stimulation site after 1 minute (Figure 5F-5G and Supplemental Figures S9, S10). On the other hand, with Stargazin-iLID, we observed stronger localized recruitment that remained more sharply localized over time, with higher signal at the stimulation site and markedly reduced signal at distal regions (Figure 5F-5G, and Supplemental Figures S9, S10).

Given the complexity of cell signaling pathways, we also wanted to determine whether the more localized recruitment could translate to sharper confinement of signaling activity over biologically-relevant timescales. To this end, we used iLID to activate signaling by the Rho family GTPase Rac1, which is an important regulator of cytoskeletal rearrangements often targeted in optogenetic studies. By fusing SspB to the catalytic DH-PH domain of the guanine nucleotide exchange factor (GEF) Tiam1, optogenetic membrane recruitment is sufficient to activate Rac1 and promote actin-based membrane protrusion. Using iLID-CAAX or Stargazin-iLID, repeated cell edge stimulation every 10 seconds for 10 minutes led to long-term Tiam1-SspB recruitment and resulted in the formation of both stable protrusions and transient membrane ruffles (Figure 5H and Supplementary Movie S5, S6). We assessed the spatial confinement of these shape changes by calculating the sum of the protrusion area over the course of the experiment and determining the percentage of this total that was confined within a fixed-size region of interest (ROI) around the stimulation spot. Consistent with our previous findings, protrusions were more locally constrained upon recruitment with Stargazin-iLID compared to iLID-CAAX. (Figure 5I).

Ultimately, our results demonstrate that Stargazin-iLID is ideally suited for subcellular protein recruitment, as the construct expresses well and the large N-terminal transmembrane anchor allows stronger recruitment and increases confinement of signaling activity through slower lateral diffusion.

3.5 Discussion

Light-inducible dimers are highly flexible systems in a growing molecular toolkit for perturbing signaling networks in ever-more precise ways. With their acute spatial and temporal control, local signaling motifs such as feedback loops can be directly probed [36]. Additionally, by adjusting light intensity, the appropriate amount of protein can be recruited to best suit the signaling system under investigation. However, these benefits are diminished by variable protein expression and diffusion, which limit the ability to reliably recruit the desired amount of protein to an exact subcellular location. In this study, we present alternative iLID fusion proteins that display stronger recruitment with higher spatial confinement across a wider range of component expression levels when compared to the commonly used version. In doing so, we relied upon a combination of quantitative imaging and mathematical modeling. We found that experimental and conceptual approaches were both needed to dissect the combined influences of protein fusion configuration, diffusion, and component expression levels on optogenetic system performance. The use of automation in our live cell imaging approaches was critical for maximizing biological replicates and improving experimental reproducibility. This allowed us to assess each system quantitatively and draw direct comparisons to our mathematical model predictions. Based on our findings, Table 1 summarizes the iLID constructs and relative component concentrations that we recommend for different optogenetic applications.

Our alternative iLID fusion proteins offer a simple and adaptable way to improve local protein recruitment. Indeed, a key benefit to our approach is that different constructs can easily be interchanged depending on the specific requirements for a given experiment. Some caveats should be noted, however. First, while we did not observe nonspecific effects in HEK293T cells, Stargazin and ADRB2 do have

biological activities, and their overexpression could have unintended biological effects in some contexts. Second, we recognize that our fusion proteins do not eliminate the issue of diffusion altogether, and other strategies have been put forward. For instance, efforts to engineer iLID and SspB variants with higher dissociation rate constants could improve spatial confinement, and one mutant protein with an altered dimer lifetime has been described [24]. However, with fast dissociation, the total amount of recruited protein is diminished, and some downstream signaling processes that require longer activation times may not be triggered [26,37]. Alternatively, Van Geel et al. restricted iLID diffusion directly using Cry2-based clustering of C2 domains or simultaneous anchoring to both membrane and microtubules [38]. Their strategies greatly reduced iLID mobility through the membrane but come with their own potential drawbacks. Heterogeneity in Cry2 expression and non-uniformity in microtubule positioning could diminish experimental reproducibility within their system, and intentional clustering of recruited molecules and perturbations to microtubule dynamics could also alter biological outputs. Ultimately, the simplicity and overall effectiveness of our anchoring strategies make them an ideal option for subcellular optogenetic applications.

Aside from slowed diffusion, we observed a clear increase in fold recruitment when we switched from a C-terminal to N-terminal anchoring strategies. We hypothesize that moving the anchor away from the intermolecular binding interface may increase flexibility or alleviate steric hindrance that limits interactions between SspB and iLID-CAAX. If so, including a longer flexible linker after the Jα helix may allow stronger recruitment using a C-terminal anchor, though this has not been tested. Additionally, it is possible that the CAAX anchor configuration also plays a beneficial role in helping to prohibit dark-state iLID-SspB binding, which our N-terminal anchoring strategies may eliminate. While our TIRF data does not allow us to directly assess the extent of basal iLID-SspB binding, it does suggest that, on average, similar amounts of basal SspB are observed proximal to the cell membrane for all constructs. iLID's LOV2 domain also contains a conserved N-terminal helix-turn-helix motif that engages in direct intramolecular interactions involved in photoswitching [39]. Whether our N-terminal anchors affect these interactions is also unknown. In the future, determining the structural consequences of the various anchoring strategies may guide efforts to engineer iLID variants with even more precise photoswitching properties.

An unexpected benefit of our slow-diffusing iLID constructs is an increased expression range for which effective recruitment is still possible. A main difference between fast- and slow-diffusing proteins is a large increase in the range of iLID expression levels for which fold-change in recruitment remains high. Indeed, we frequently observed small fold changes in recruitment with the original iLID-CAAX system, which can likely be explained by the presence of only a small sub-population of cells with iLID expression levels that appropriately balance basal and light-activated recruitment. Finally, in all scenarios, we observed large changes in both basal and absolute recruitment over relatively small differences in component concentrations (Supplemental Figure S11). While our slow-diffusing constructs are more robust in cell populations with variable protein levels, care should be taken to minimize heterogenous expression by using stable rather than transient expression methods. Overall, our findings demonstrate the importance of considering the requirements for protein recruitment for different applications, and our model provides general guidelines for optimizing component expression patterns accordingly.

We expect that our alternative iLID fusion proteins will enable more precise subcellular recruitment and broaden the range of applications for which iLID can be used. Furthermore, the principles highlighted by our mathematical models will ensure greater reproducibility within and between research groups using iLID for light-based protein recruitment.

3.6 Methods

3.6.1 Cell culture

HEK-293T cells were obtained from the laboratory of Lifeng Xu and cultured in high glucose DMEM medium with sodium bicarbonate (Sigma-Aldrich catalog no D5671) and supplemented with 10% FBS, 1% penicillin and streptomycin, and 1% GlutaMax (Thermo Fisher catalog no 35050061) in a humidified incubator at 37° C and 5% atmospheric CO_2. Cells were maintained at a density between 10% and 80% confluency on untreated 6-well tissue culture plates.

3.6.2 Constructs

pLL7.0:Venus-iLID-CAAX (from KRas4B), pLL7.0:tgRFPt-SSPB WT, and pLL7.0:mTiam1(64-437)-tgRFPt-SspB R73Q were gifts from Brian Kuhlman (Addgene plasmid # 60411; http://n2t.net/addgene:60411; RRID:Addgene_60411, Addgene plasmid # 60415; http://n2t.net/addgene:60415; RRID:Addgene_60415, and Addgene plasmid # 60418; http://n2t.net/addgene:60418; RRID:Addgene_60418) [12]. Stargazin-GFP-LOVpep was a gift from Michael Glotzer (Addgene plasmid # 80406; http://n2t/net/addgene:80406; RRID:Addgene_80406) [33]. Beta-2-adrenergic receptor-CFP was a gift from Catherine Berlot (Addgene plasmid # 55794; http://n2t.net/addgene:55794; RRID:Addgene_55794) [40]. To generate the iLID plasmids, mTurqouise2, iLID-CAAX, iLID (no CAAX), the N-terminal myristoylated/palmitoylated domain of human Lyn tyrosine kinase (1-11), full-length Stargazin, and full-length ADRB2 were PCR amplified. Additionally, a modified version of the influenza hemagglutinin signal sequence (residues 2-16) was generated by oligonucleotide annealing for insertion upstream of the ADRB2 sequence to enhance membrane localization. Consistent with the original Venus-iLID-CAAX construct, a short flexible linker (Gly-Ser-Gly-Ser-Gly-Glu-Phe) was included between mTurquoise2 and iLID in all constructs. Flexible linkers were also included between iLID and CAAX (Gly-Ser-Gly-Ser-Gly-Ser) and Lyn11 and mTurqouise2 (Gly-Ala-Asp-Ser-Ala-Gly-Ser-Ala-

Gly-Ser-Ala-Gly). Gene fragments were cloned via Gibson assembly into a lentiviral backbone containing an upstream ubiquitous chromatin opening element (UCOE), EF1-a promoter, and the blasticidin resistance gene downstream of an IRES sequence. For generating the tdTomato-SspB plasmid, td-Tomato, SspB, and iRFP-670 were PCR amplified. A tandem P2A/T2A sequence (tPT2A) reported by Liu et al. was synthesized using Twist Biosciences' fragmentGene service [41]. Gene fragments were cloned via Gibson assembly into a lentiviral backbone containing the EF1-a promoter and the puromycin resistance gene downstream of an IRES sequence. The downstream PT2A-iRFP-670 element allows for co-expression of iRFP-670 as a reference cytoplasmic marker if needed. For generating the mTiam1(DH-PH)-mCitrine-SspB plasmid, the DH-PH domain of mTiam1, mCitrine, and SspB were PCR amplified and cloned via Gibson assembly into a lentiviral backbone containing the EF1-a promoter and puromycin resistance gene downstream of an IRES sequence. Constructs were stably co-expressed in HEK-293T cells via subsequent rounds of lentivirus transduction and antibiotic selection.

3.6.3 Automated TIRF Microscopy

Cells were plated on glass bottom 96-well plates (Cellvis catalog no P96-1.5H-N) treated with 200 ug/ml poly-D-lysine (Sigma-Aldrich catalog #P6407) and allowed to grow at 37° C and 5% atmospheric CO_2 for ~16 hours. TIRF images were acquired using a Nikon Ti-E inverted fluorescence microscope with a 60x 1.49 NA Apo TIRF oil immersion objective and an Andor Zyla 4.2 sCMOS camera at 37° C. To minimize user bias and cell-to-cell variability, custom software was written for automated cell selection, cell stimulation and time lapse imaging using a MATLAB interface for Micro-manager. Briefly, each well was organized into an x-y matrix of locations that were imaged consecutively. At each location, a reference TIRF image was captured, and a correction was applied for non-uniform illumination of the TIRF field. From this, cell segmentation was performed using a minimum fluorescence threshold and minimum and maximum size thresholds. Cell masks were used to identify the cell with the highest area-to-perimeter ratio and move to its centroid coordinate. Area-to-perimeter ratio served as a suitable metric for selecting spread out cells with simple geometries. Finally, automated cell stimulation and time lapse imaging was carried

out before moving to the next location. For single point-stimulation experiments and global illumination experiments, images were acquired every 1 second for 25 frames, and a single 10 ms pulse of 445 nm light was applied between frames 5 and 6. For multi-stimulation experiments, images were acquired every 2 seconds for 33 frames, and a 10 ms pulse of 445 nm light was applied after frames 3, 8, 13, 18, 23, 28, and 32. Finally, for Tiam1 recruitment experiments, images were acquired every 20 seconds for 33 frames, and a 10 ms pulse of 445 nm light was applied every 10 seconds beginning after frame 3. Global iLID activation was achieved using a 445 nm LED. Subcellular iLID activation was achieved using a 445 nm laser connected to a Nikon FRAP illumination module with an ND 2.0 (1% transmission) neutral density filter in the light path. At the end of each experiment, a single TIRF image was acquired using a 445 nm laser to visualize iLID protein at the cell membrane.

3.6.4 Determination of stimulus location for point-recruitment experiments

All imaging processing and analysis was performed using MATLAB. The stimulus location for point-recruitment experiments was estimated to be near the x-y center of the SspB fluorescence images, but the exact location could vary by a few pixels from day to day. Therefore, to determine the exact stimulus location for each day, the following empirical method was used. After image acquisition, cells with iLID fluorescence intensity below a minimum threshold, which was set manually based on background intensity, were excluded from analysis. Next, each movie was viewed in a randomized order and cells showing recruitment near the cell edge were eliminated. Remaining cells were used to generate a stimulus spot mask. For each cell, we performed a pixel-by-pixel subtraction of the raw 2 second post-stimulation SspB fluorescence image from the raw 1 second pre-stimulation SspB fluorescence image. The resulting images were composited, a rough stimulus spot mask was generated by masking for the brightest 20% of pixels, then a final stimulus spot mask was generated by finding the centroid coordinates of the rough mask and dilating the mask to a circle with a radius of 5 pixels (~1 mm).

3.6.5 Background subtraction and cell segmentation of TIRF images

TIRF images were processed by performing local background subtraction and cell segmentation using previously described methods [3]. Briefly, corrections were applied to raw fluorescence images to account for minor camera-specific artifacts and aberrations in the light-path. Background pixels were isolated by performing an initial conservative cell segmentation to remove high intensity pixels with fluorescence from cells or other objects. From the resulting background image, local background values were assigned by calculating the median intensity of pixels within defined 200x200 pixel blocks, then smoothing was applied to remove hard edges and generate a smooth background image. Next, cell masks were generated from the first SspB fluorescence image from each experiment. A single mask was suitable because no discernable changes to cell shape or location took place during individual experiments. To generate cell masks, smoothing was applied using a Gaussian filter of width 5 pixels (1.1 mm) to reduce pixel noise. Next, cell edges were enhanced using unsharp masking. Cell masks were generated using automated pixel thresholding followed by morphological closing (mask dilation followed by erosion), removal of small non-cell (<100 mm^2) objects, and removal of masks of non-stimulated cells. For Tiam1 recruitment experiments, automated pixel thresholding was not robust in capturing fine cell shape changes. Therefore, a semi-automated thresholding approach was designed. Experiments were randomized to eliminate bias, and a threshold value for each cell was manually determined based on example images generated using a range of pre-set threshold values.

3.6.6 Analysis of iLID and SspB intensity from TIRF images

Cells used to generate stimulus spot masks were included for analysis of iLID fluorescence intensity and SspB recruitment. To calculate iLID fluorescence intensities, background subtraction was performed as described above. iLID images were then computationally registered to SspB images using x and y translations. Images were smoothed with a Gaussian filter of width 2 pixels (0.32 mm) to reduce pixel noise and segmentation was performed by applying the previously generated cell masks. Finally, iLID fluorescence intensity was measured as the mean intensity of pixels within the stimulus spot mask. To

calculate SspB florescence intensities, background subtraction and pixel smoothing were performed, and previously generated cell masks were applied. Basal SspB fluorescence intensity was measured as the mean intensity of pixels within the stimulus spot mask. For recruitment analysis, images were normalized to pre-stimulus levels by dividing each post-stimulation image by a reference 1 second pre-stimulation image on a pixel-by-pixel basis. SspB fluorescence intensity at the stimulation spot at each timepoint was calculated as the mean intensity of pixels within the stimulus spot mask. To calculate SspB signal for cell groups with different iLID levels (Figures 4G-4H), cells with basal SspB above 5,000 (AU) were eliminated to remove outliers. Cells were then binned into five groups based on iLID fluorescence intensity such that the magnitude of the recruitment curves were well-separated, and mean time courses were calculated for each group.

3.6.7 Analysis of spatial SspB intensity gradients from TIRF images

The same images used for recruitment analysis were also used for spatial analysis, with the same image processing, smoothing, masking, and normalization applied. Using the stimulus spot masks and each cell mask, we first calculated the geodesic distance of each pixel in the cell mask from the site of stimulation, and grouped pixels based on distance values into bins of width 1.5 pixel (~0.32 mm). We then calculated the mean SspB intensity for each bin over time. The half-maximum of the gradient signal was calculated as the average of the maximum and minimum values of the gradient, and the distance for half-maximal signal was taken to be the distance of the gradient data point closest to the half-maximum value. Finally, spatial spread values were determined by calculating the fold change in half-maximum distance between 1 and 10 seconds post-stimulation (frames 6 and 16, respectively).

3.6.8 Analysis of membrane protrusion

Protrusion analysis was restricted to the stimulated half of each cell, as segmentation was not as precise on the distal half where signal-to-noise was low. Cell protrusions were identified by performing a pixel-by-pixel subtraction of each half-mask from the initial post-stimulation half-mask and removing negative (retracting) regions. The post-stimulation half-mask was used as the reference to avoid possible

systematic biases in segmentation due to light-induced increases in fluorescence intensity. Protrusion areas throughout the course of each experiment were then summed. An ROI was automatically defined as a rectangle of width 100 pixels (~21 mm) and height 150 pixels (~32 mm) and its center at the cell edge location closest to the stimulation site. Protrusion confinement was quantified by calculating the percentage of the summed protrusion area that was found within the ROI. Importantly, the results of our analysis were consistent when other ROI sizes were used.

3.6.9 Confocal Microscopy

Lyn11-iLID cells were used to study cytosolic SspB recovery via confocal microscopy. For iLID FRAP experiments, cells expressing iLID constructs without SspB were used. Cells were plated on glass bottom 96-well plates as described above. Confocal images were acquired using an Intelligent Imaging Innovations spinning disk confocal microscope using either a 40x 1.3 NA Fluar oil immersion objective and Hamamatsu ORCA-Flash4.0 V2 sCMOS camera (SspB recovery experimrnts) or 100x oil immersion objective and QuantEM 512SC EMCCD camera (FRAP experiments) at 37° C. Time lapse imaging was conducted using 3i Slidebook6 software. For SspB recovery experiments, images were acquired every 1 second for 1 minute using a 561 nm laser. Visualization and photoactivation of iLID was performed by acquiring a single confocal image using a 445 nm laser. For iLID FRAP experiments, images were acquired every 200 ms for 35 seconds using a 445 nm laser. Photobleaching was achieved by scanning a 5 mm^2 region with high-intensity 488 nm light between frames 25 and 26.

3.6.10 Analysis of cytoplasmic SspB recovery using confocal microscopy

Cytoplasmic SspB image data was read into MATLAB using the Open Microscopy Environment's Bio-Formats 6.1.0 toolbox. Time courses were analyzed in a randomized order to eliminate bias. For each time course experiment, we computed the fold change in SspB intensity from 1 second before to 3 seconds after stimulation on a pixel-by-pixel basis. Cytoplasmic areas of cells that responded to light stimulation were identified as large (>3.8 mm^2) regions that showed at least 1% loss in pixel intensity over the chosen time frame. Next, a 25 pixel (~0.5 μm^2) region of interest (ROI) was manually selected from each

cytoplasmic area to ensure that cell edges and internal structures were not included in our analysis. Single cell intensity measurements were calculated as the mean SspB intensities of the ROIs at each time point. The non-normalized pre-stimulus SspB intensity was used to estimate total SspB abundance in each cell, and the percent loss in SspB intensity at 4 seconds post-stimulation (the time of peak recruitment for most cells) was used to estimate total iLID abundance. To assess recruitment and recovery kinetics at different component ratios, cells were binned into four groups of similarly sized ratio intervals, and average time courses were calculated.

3.6.11 Analysis of iLID FRAP

Confocal FRAP data was analyzed using MATLAB. The recovery of iLID fluorescence was calculated as a function of distance from the bleach center. First, ROIs of the cell membrane extending beyond the bleached region were manually determined using the 'drawpolyline' function in MATLAB. Unbleached regions were manually selected and used to correct for photobleaching as a result of imaging. Next, we calculated the geodesic distance of each pixel in the bleach ROI from the bleach center. Finally, pixels were grouped based on distance values into bins of width 1 pixel (~0.13 mm), and the mean iLID intensity for each bin was calculated over time. These recovery curves were used to fit a one-dimensional PDE diffusion model to estimate diffusion coefficients for each iLID construct. We used a Neumann boundary condition and used the spatial profile from the first time point as the initial condition. The model had two parameters: the diffusion coefficient, and a parameter for the distance between the edge of the ROI and the boundary where the Neumann condition was applied.

3.6.12 Mathematical modeling

All mathematical modeling was performed using code written in MATLAB. The objective of our differential equation model was to predict species concentrations over time at varying optogenetic component concentrations. Using the framework illustrated in Figure 3A, we identified five species that comprise the system: free $iLID_{dark}$, free $iLID_{lit}$, $iLID_{dark}$-SspB, $iLID_{lit}$-SspB, and free SspB. We began by defining parameters and rate constants for the activation and binding reactions based on published data.

Reported equilibrium constants of 4.7 mM (Kd_{dark}) and 130 nM (Kd_{lit}) for iLID$_{dark}$ and iLID$_{lit}$, respectively, were used [12]. The iLID-SspB association rate ($R_{assoc.}$) was assumed to be the same for both dark and lit states of iLID, the lit state dissociation rate was estimated to be 0.5 sec^{-1}, and an iLID dark-state reversion rate ($R_{rev.}$) of 0.02 sec^{-1} was chosen based on published measurements [26]. For the PDE model, we also included a diffusion coefficient parameter that could be set according to the iLID construct being modeled and a cell radius parameter that was set to 15 mm. We used a diffusion coefficient of 25 mm^2/sec for free SspB based on published estimates for cytosolic proteins [42]. Other kinetic parameters could be defined from the above:

$$R_{dissocLit} = 0.5 \ sec^{-1}$$

$$R_{assoc} = R_{dissocLit}/Kd_{lit}$$

$$R_{dissocDark} = R_{assoc} \times Kd_{dark}$$

We next determined initial conditions, assuming a steady-state in which no iLID molecules were active before stimulation. Therefore, $[initial \ free \ iLID_{lit}] = 0$ and $[initial \ iLID_{lit} - SspB] = 0$. We then used conservation of mass and equilibrium binding to compute the initial free iLID$_{dark}$, initial free SspB, and initial iLID$_{dark}$-SspB complex as follows:

$$[initial \ free \ iLID_{dark}] = [iLID_{total}] - [initial \ iLID_{dark} - SspB]$$

$$[initial \ free \ SspB] = [SspB_{total}] - [initial \ iLID_{dark} - SspB]$$

$$[initial \ iLID_{dark} - SspB] = b - \frac{\sqrt{b^2 - 4 \times [iLID_{total}] \times [SspB_{total}]}}{2},$$

where b is $[iLID_{total}] + [SspB_{total}] + Kd_{dark}$

For the PDE model, we also defined symmetry and boundary conditions to account for spatial considerations. We modeled the cell as a radially symmetric disc with membrane and cytoplasmic

compartments modeled at every radial distance from a center stimulation point to the outer cell edge, and we used a reflective boundary condition.

For the ODE model, we included a stepwise function as an input to our model to mimic global iLID stimulation, with a single stimulation pulse at the start of the model time course equivalent to 100 ms in length. We assumed that all iLID molecules were converted to their active form upon stimulation. For the PDE model, we mimicked subcellular light stimulation by generating an input function that was fit to match the spatial SspB intensity gradient 1 second after stimulation from Stargazin-iLID data, scaled to have values between 0 and 1. We refer to the solution of these input functions as Stim_{fun} in the equations below, and note that Stim_{fun} was defined to be uniformly zero at all times other than during simulated light stimulation.

Finally, we generated the following differential equations to define the concentration of each species:

(1) $\frac{d[free\ iLID_{dark}]}{dt} = (R_{rev.} \times [free\ iLID_{lit}]) + (R_{dissocDark} \times [iLID_{dark} - SspB]) - (Stim_{fun} \times$

$[free\ iLID_{dark}]) - (R_{assoc} \times [free\ iLID_{dark}] \times [free\ SspB])$

(2) $\frac{d[free\ iLID_{lit}]}{dt} = (Stim_{fun} \times [free\ iLID_{dark}]) + (R_{dissocLit} \times [iLID_{lit} - SspB]) - (R_{rev.} \times$

$[free\ iLID_{lit}]) - R_{assoc.} \times [free\ iLID_{lit}] \times [free\ SspB]$

(3) $\frac{d[iLID_{dark} - SspB]}{dt} = (R_{assoc.} \times [free\ iLID_{dark}] \times [free\ SspB]) + (R_{rev.} \times [iLID_{lit} - SspB]) -$

$(Stim_{fun} \times [iLID_{dark} - SspB]) - (R_{dissocDark} \times [iLID_{dark} - SspB])$

(4) $\frac{d[iLID_{lit} - SspB]}{dt} = (Stim_{fun} \times [iLID_{dark} - SspB]) + (R_{assoc.} \times [free\ iLID_{lit}] \times [free\ SspB]) -$

$(R_{rev.} \times [iLID_{lit} - SspB]) - (R_{dissocLit} \times [iLID_{lit} - SspB])$

(5) $\frac{d[free\ SspB]}{dt} = R_{dissocLit} \times [iLID_{lit} - SspB] + R_{dissocDark} \times [iLID_{dark} - SspB] - R_{assoc.} \times$

$[free\ iLID_{lit}] \times [free\ SspB] - R_{assoc.} \times [free\ iLID_{dark}] \times [free\ SspB]$

To run our model calculations, we used a first-order ODE solver (the ode45 function in MATLAB) and a 1-D PDE solver (the pdepe function in MATLAB) for the ODE and PDE versions of the model, respectively. A 1-D solver was appropriate for our PDE model given the radial symmetry of the system.

3.6.13 Statistics

Statistical analyses were carried out in MATLAB. For Figure 2B-2D, Figure 3I, Figure 5E, Figure 5I, Supplemental Figure S2, and Supplemental Figure S8, significance was calculated using the Mann-Whitney U test (ranksum function in MATLAB) to compare values from each construct to iLID-CAAX. For Figure 2E-2H and Supplemental Figure S4, significance was calculated using a permutation test with 10,000 random permutations per set of conditions. All results in this study were independently replicated at least three times, except for iLID FRAP analysis, for which two independent replicates were carried out.

3.7 Data availability

Raw datasets and analysis code are available upon request.

3.8 Acknowledgements

3.9 Funding sources

3.10 Conflict of interest

The authors declare no conflicts of interest.

3.11 References

(1)   Yüce, Ö., Piekny, A., Glotzer, M. (2005) An ECT2-Centralspindlin Complex Regulates the Localization and Function of RhoA. *J. Cell Biol. 170* (4), 571–582. https://doi.org/10.1083/jcb.200501097.

(2)   Janetopoulos, C., Ma, L., Devreotes, P. N., Iglesias, P. A. (2004) Chemoattractant-Induced Phosphatidylinositol 3,4,5-Trisphosphate Accumulation Is Spatially Amplified and Adapts, Independent of the Actin Cytoskeleton. *Proc. Natl. Acad. Sci. U. S. A. 101* (24), 8951–8956. https://doi.org/10.1073/pnas.0402152101.

(3)   Yang, H. W., Collins, S. R., Meyer, T. (2016) Locally Excitable Cdc42 Signals Steer Cells during Chemotaxis. *Nat. Cell Biol. 18* (2), 191–201. https://doi.org/10.1038/ncb3292.

(4)   Reinhard, N. R., Mastop, M., Yin, T., Wu, Y., Bosma, E. K., Gadella, T. W. J., Goedhart, J., Hordijk, P. L. (2017) The Balance between Gαi-Cdc42/Rac and Gα12/13 -RhoA Pathways Determines Endothelial Barrier Regulation by Sphingosine-1-Phosphate. *Mol. Biol. Cell 28* (23), 3371–3382. https://doi.org/10.1091/mbc.E17-03-0136.

(5)   Singleton, K. L., Roybal, K. T., Sun, Y., Fu, G., Gascoigne, N. R. J., Van Oers, N. S. C., Wülfing, C. (2009) Spatiotemporal Patterning during T Cell Activation Is Highly Diverse. *Sci. Signal. 2* (65), 1–13. https://doi.org/10.1126/scisignal.2000199.

(6)   Brandman, O., Tobias. (2008) Feedback Loops Shape Cellular Signals in Space and Time. *Science (80-.). 322* (5900), 390–395. https://doi.org/10.1126/science.1160617.Feedback.

(7)   Guilluy, C., Garcia-Mata, R., Burridge, K. (2011) Rho Protein Crosstalk: Another Social Network? *Trends Cell Biol. 21* (12), 718–726. https://doi.org/10.1016/j.tcb.2011.08.002.

(8)   Yazawa, M., Sadaghiani, A. M., Hsueh, B., Dolmetsch, R. E. (2009) Induction of Protein-Protein Interactions in Live Cells Using Light. *Nat. Biotechnol. 27* (10), 941–945. https://doi.org/10.1038/nbt.1569.

(9)   Levskaya, A., Weiner, O. D., Lim, W. A., Voigt, C. A. (2009) Spatiotemporal Control of Cell Signalling Using a Light-Switchable Protein Interaction. *Nature 461* (7266), 997–1001. https://doi.org/10.1038/nature08446.

(10)   Kennedy, M. J., Hughes, R. M., Peteya, L. A., Schwartz, J. W., Ehlers, M. D., Tucker, C. L. (2010) Rapid Blue-Light-Mediated Induction of Protein Interactions in Living Cells. *Nat. Methods 7* (12), 973–977. https://doi.org/10.1038/nmeth.1524.

(11)   Strickland, D., Lin, Y., Wagner, E., Hope, C. M., Zayner, J., Antoniou, C., Sosnick, T. R., Weiss, E. L., Glotzer, M. (2012) TULIPs: Tunable, Light-Controlled Interacting Protein Tags for Cell Biology. *Nat. Methods 9* (4), 379–384. https://doi.org/10.1038/nmeth.1904.

(12)   Guntas, G., Hallett, R. a., Zimmerman, S. P., Williams, T., Yumerefendi, H., Bear, J. E., Kuhlman, B. (2015) Engineering an Improved Light-Induced Dimer (ILID) for Controlling the Localization and Activity of Signaling Proteins. *Proc. Natl. Acad. Sci. 112* (1), 112–117. https://doi.org/10.1073/pnas.1417910112.

(13)   Grecco, H. E., Schmick, M., Bastiaens, P. I. H. (2011) Signaling from the Living Plasma Membrane. *Cell 144* (6), 897–909. https://doi.org/10.1016/j.cell.2011.01.029.

(14)   Parent, C. A., Blacklock, B. J., Froehlich, W. M., Murphy, D. B., Devreotes, P. N. (1998) G Protein Signaling Events Are Activated at the Leading Edge of Chemotactic Cells. *Cell 95* (1), 81–91. https://doi.org/10.1016/S0092-8674(00)81784-5.

(15)   Iijima, M., Devreotes, P. (2002) Tumor Suppressor PTEN Mediates Sensing of Chemoattractant

Gradients. *Cell 109*, 599–610.

(16)   Xu, J., Wang, F., Van Keymeulen, A., Herzmark, P., Straight, A., Kelly, K., Takuwa, Y.,

Sugimoto, N., Mitchison, T., Bourne, H. R. (2003) Divergent Signals and Cytoskeletal Assemblies

Regulate Self-Organizing Polarity in Neutrophils. *Cell 114* (2), 201–214.

https://doi.org/10.1016/S0092-8674(03)00555-5.

(17)   Dougan, D. A., Weber-ban, E., Bukau, B., Heidelberg, B. (2003) Targeted Delivery of an SsrA-

Tagged Substrate by the Adaptor Protein SspB to Its Cognate AAA+ Protein ClpX. *Mol. Cell 12*,

373–380.

(18)   Rafelski, S. M., Theriot, J. A. (2006) Mechanism of Polarization of Listeria Monocytogenes

Surface Protein ActA. *Mol. Microbiol. 59* (4), 1262–1279. https://doi.org/10.1111/j.1365-

2958.2006.05025.x.

(19)   Weiner, O. D., Marganski, W. A., Wu, L. F., Altschuler, S. J., Kirschner, M. W. (2007) An Actin-

Based Wave Generator Organizes Cell Motility. *PLoS Biol. 5* (9), 2053–2063.

https://doi.org/10.1371/journal.pbio.0050221.

(20)   Tischer, D., Weiner, O. D. (2014) Illuminating Cell Signalling with Optogenetic Tools. *Nat. Rev.

Mol. Cell Biol. 15* (8), 551–558. https://doi.org/10.1038/nrm3837.

(21)   O'Neill, P. R., Kalyanaraman, V., Gautam, N. (2016) Subcellular Optogenetic Activation of

Cdc42 Controls Local and Distal Signaling to Drive Immune Cell Migration. *Mol. Biol. Cell 27*

(9), 1442–1450. https://doi.org/10.1091/mbc.E15-12-0832.

(22)   Johnson, H. E., Goyal, Y., Pannucci, N. L., Sch, T., Shvartsman, S. Y., Toettcher, J. E.,

Shvartsman, S. Y. (2017) The Spatiotemporal Limits of Developmental Erk Signaling. *Dev. Cell

40*, 185–192. https://doi.org/10.1016/j.devcel.2016.12.002.

(23)   Okumura, M., Natsume, T., Kanemaki, M. T., Kiyomitsu, T. (2018) Dynein–Dynactin–NuMA

Clusters Generate Cortical Spindle-Pulling Forces as a Multiarm Ensemble. *Elife 7*, 1–24.

https://doi.org/10.7554/eLife.36559.

(24)   Zimmerman, S. P., Hallett, R. A., Bourke, A. M., Bear, J. E., Kennedy, M. J., Kuhlman, B. (2016)

Tuning the Binding Affinities and Reversion Kinetics of a Light Inducible Dimer Allows Control of Transmembrane Protein Localization. *Biochemistry 55* (37), 5264–5271. https://doi.org/10.1021/acs.biochem.6b00529.

(25)   Toettcher, J. E., Gong, D., Lim, W. A., Weiner, O. D. (2011) Light-Based Feedback for Controlling Intracellular Signaling Dynamics. *Nat. Methods 8* (10), 837–839. https://doi.org/10.1038/nmeth.1700.

(26)   Benedetti, L., Barentine, A. E. S., Messa, M., Wheeler, H., Bewersdorf, J., De Camilli, P. (2018) Light-Activated Protein Interaction with High Spatial Subcellular Confinement. *Proc. Natl. Acad. Sci. U. S. A. 115* (10), E2238–E2245. https://doi.org/10.1073/pnas.1713845115.

(27)   Apolloni, A., Prior, I. A., Lindsay, M., Parton, R. G., Hancock, J. F. (2000) H-Ras but Not K-Ras Traffics to the Plasma Membrane through the Exocytic Pathway. *Mol. Cell. Biol. 20* (7), 2475–2487. https://doi.org/10.1128/mcb.20.7.2475-2487.2000.

(28)   Das, S., Yin, T., Yang, Q., Zhang, J., Wu, Y. I., Yu, J. (2015) Single-Molecule Tracking of Small Gtpase RAC1 Uncovers Spatial Regulation of Membrane Translocation and Mechanism for Polarized Signaling. *Proc. Natl. Acad. Sci. U. S. A. 112* (3), E267–E276. https://doi.org/10.1073/pnas.1409667112.

(29)   Meder, D., Moreno, M. J., Verkade, P., Vaz, W. L. C., Simons, K. (2006) Phase Coexistence and Connectivity in the Apical Membrane of Polarized Epithelial Cells. *Proc. Natl. Acad. Sci. U. S. A. 103* (2), 329–334. https://doi.org/10.1073/pnas.0509885103.

(30)   Kovářová, M., Tolar, P., Arudchandran, R., Dráberová, L., Rivera, J., Dráber, P. (2001) Structure-Function Analysis of Lyn Kinase Association with Lipid Rafts and Initiation of Early Signaling Events after Fcε Receptor I Aggregation. *Mol. Cell. Biol. 21* (24), 8318–8328. https://doi.org/10.1128/mcb.21.24.8318-8328.2001.

(31)   Letts, V. A., Felix, R., Biddlecome, G. H., Arikkath, J., Mahaffey, C. L., Valenzuela, A., Bartlett, F. S., Mori, Y., Campbell, K. P., Frankel, W. N. (1998) The Mouse Stargazer Gene Encodes a Neuronal Ca2+-Channel γ Subunit. *Nat. Genet. 19* (4), 340–347. https://doi.org/10.1038/1228.

(32)   Bang, I., Choi, H. J. (2015) Structural Features of B2 Adrenergic Receptor: Crystal Structures and Beyond. *Mol. Cells 38* (2), 105–111. https://doi.org/10.14348/molcells.2015.2301.

(33)   Wagner, E., Glotzer, M. (2016) Local RhoA Activation Induces Cytokinetic Furrows Independent of Spindle Position and Cell Cycle Stage. *J. Cell Biol. 213* (6), 641–649. https://doi.org/10.1083/jcb.201603025.

(34)   Rich, A., Fehon, R. G., Glotzer, M. (2020) Rho1 Activation Recapitulates Early Gastrulation Events in the Ventral, but Not Dorsal, Epithelium of Drosophila Embryos. *Elife 48*, 1–22. https://doi.org/10.1101/2020.03.12.989285.

(35)   Yanagawa, M., Hiroshima, M., Togashi, Y., Abe, M., Yamashita, T., Shichida, Y., Murata, M., Ueda, M., Sako, Y. (2018) Single-Molecule Diffusion-Based Estimation of Ligand Effects on G Protein-Coupled Receptors. *Sci. Signal. 11* (548), 1–16. https://doi.org/10.1126/scisignal.aao1917.

(36)   Lamas, I., Merlini, L., Vještica, A., Vincenzetti, V., Martin, S. G. *Optogenetics Reveals Cdc42 Local Activation by Scaffold-Mediated Positive Feedback and Ras GTPase*; Vol. 18. https://doi.org/10.1371/journal.pbio.3000600.

(37)   Tummino, P. J., Copeland, R. A. (2008) Residence Time of Receptor - Ligand Complexes and Its Effect on Biological Function. *Biochemistry 47* (20), 5481–5492. https://doi.org/10.1021/bi8002023.

(38)   Van Geel, O., Hartsuiker, R., Gadella, T. W. J. (2018) Increasing Spatial Resolution of Photoregulated GTPases through Immobilized Peripheral Membrane Proteins. *Small GTPases 00* (00), 1–10. https://doi.org/10.1080/21541248.2018.1507411.

(39)   Halavaty, A. S., Moffat, K. (2007) N- and C-Terminal Flanking Regions Modulate Light-Induced Signal Transduction in the LOV2 Domain of the Blue Light Sensor Phototropin 1 from Avena Sativa. *Biochemistry 46* (49), 14001–14009. https://doi.org/10.1021/bi701543e.

(40)   Hynes, T. R., Mervine, S. M., Yost, E. A., Sabo, J. L., Berlot, C. H. (2004) Live Cell Imaging of Gs and the B2-Adrenergic Receptor Demonstrates That Both As and β 1γ7 Internalize upon Stimulation and Exhibit Similar Trafficking Patterns That Differ from That of the B2-Adrenergic

Receptor. *J. Biol. Chem. 279* (42), 44101–44112. https://doi.org/10.1074/jbc.M405151200.

(41)   Liu, Z., Chen, O., Wall, J. B. J., Zheng, M., Zhou, Y. (2017) Systematic Comparison of 2A

Peptides for Cloning Multi-Genes in a Polycistronic Vector. *Sci. Rep. 7* (2193), 1–9.

https://doi.org/10.1038/s41598-017-02460-2.

(42)   Swaminathan, R., Hoang, C. P., Verkman, A. S. (1997) Photobleaching Recovery and Anisotropy

Decay of Green Fluorescent Protein GFP-S65T in Solution and Cells: Cytoplasmic Viscosity

Probed by Green Fluorescent Protein Translational and Rotational Diffusion. *Biophys. J. 72* (4),

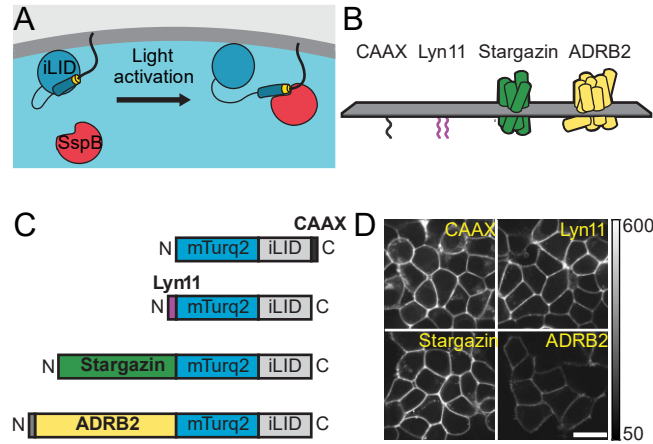1900–1907. https://doi.org/10.1016/S0006-3495(97)78835-0.

3.12 Figures

FIGURE 1

Figure 3.1. Overview of anchoring strategies for iLID fusion proteins.

(A) Schematic of iLID-based membrane recruitment. The Jα helix is depicted as a blue-gray cylinder, the SsrA peptide is shown in yellow, and the Kras CAAX domain is depicted as a bold black line. (B) Illustration of anchors used to target iLID to the plasma membrane. The CAAX and Lyn11 sequences are membrane anchored via one and two lipid groups, respectively, while Stargazin and ADRB2 are four-pass and seven-pass transmembrane anchors, respectively. (C) Domain diagrams depicting the relative sizes and configurations of the iLID fusion proteins. (D) Comparison of localization of iLID constructs in HEK293T cells visualized by confocal microscopy. Imaging settings were kept consistent across constructs for easy comparison of relative brightness. Scale bar is 20 mm.
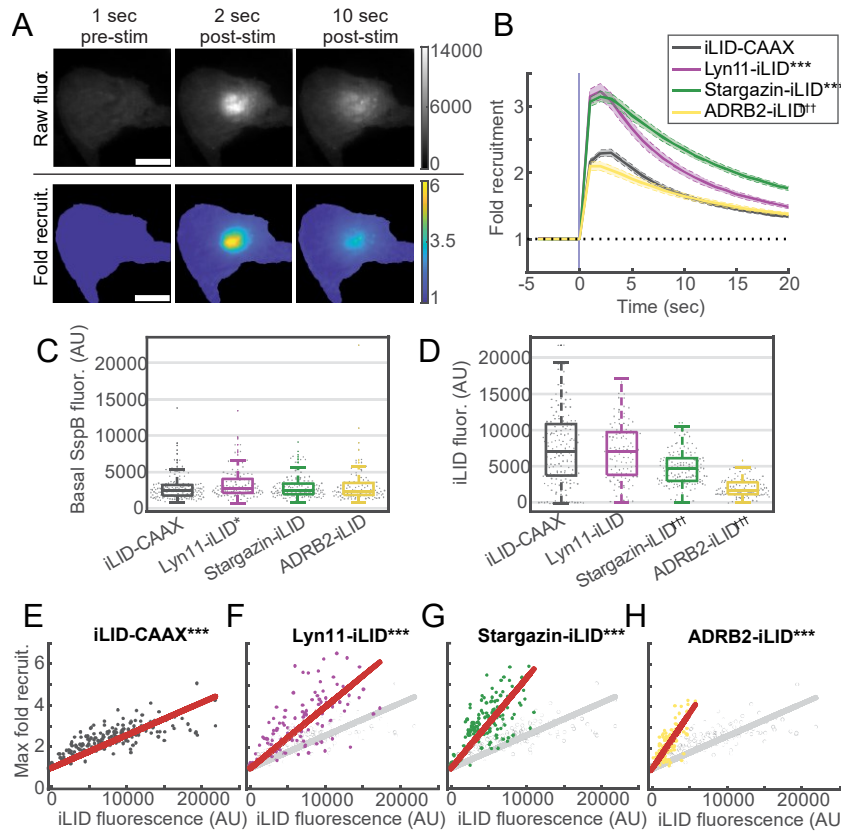
FIGURE 2

Figure 3.2. Analysis of recruitment magnitude via TIRF point-recruitment assay.

(A) Example TIRF images of tdTom-SspB recruitment to the cell membrane before (left column) and after (middle and right columns) point-stimulation with a 10 ms pulse of 445 nm light. Top row shows raw fluorescence images and bottom row shows fold change in signal. Depicted cell expresses Lyn11-iLID. Scale bar is 15 mm. (B) Plots showing mean fold change in SspB signal at the stimulation site over time for each iLID construct, normalized to pre-stimulation levels. Error bars indicate ±S.E.M. (n=166 cells for iLID-CAAX, n=115 cells for Lyn11-iLID, n=144 cells for Stargazin-iLID, n=113 cells for ADRB2-iLID).***P<0.001 for maximum recruitment values above that of iLID-CAAX. †††P<0.001 for maximum recruitment values below that of iLID-CAAX. P-values were calculated using the Mann-Whitney U test. (C-D) Box plots of average basal SspB fluorescence (C) or average iLID fluorescence (D) for each iLID construct. Central line indicates the median, bottom and top box edges indicate 25th and 75th percentiles,

and whiskers indicate most extreme data points not considering outliers. Gray dots show distributions of single cell values (n=163 cells for iLID-CAAX, n=113 cells for Lyn11-iLID, n=143 cells for Stargazin-iLID, n=113 cells for ADRB2-iLID). *P<0.05 for values above that of iLID-CAAX. [†††]P<0.001 for values below that of iLID-CAAX. P-values were calculated using the Mann-Whitney U test. (E-H). Scatterplots showing the correlation between iLID fluorescence and maximum fold recruitment in single cells. Red lines indicate the least-squares fit lines. For F-H, data from iLID-CAAX is shown in gray for easy comparison (n=163 cells for iLID-CAAX, n=113 cells for Lyn11-iLID, n=143 cells for Stargazin-iLID, n=113 cells for ADRB2-iLID). ***P<0.001 for best fit slope values that are significantly different from slope values of all other conditions. P-values were calculated using a permutation test with 10,000 random permutations.
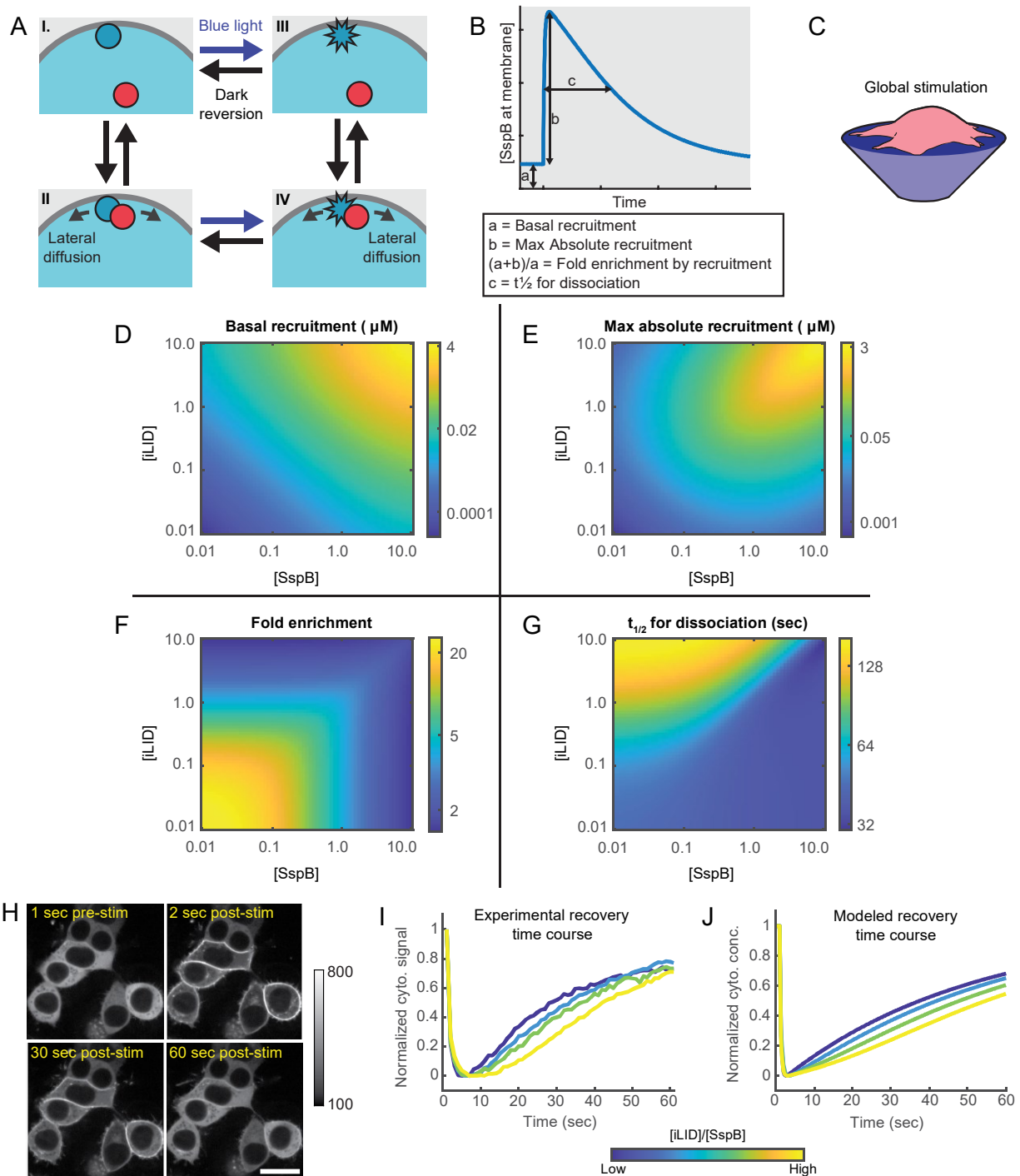
FIGURE 3

Figure 3.3. Overview of optimal expression regimes for global recruitment.

(A) Schematic diagram illustrating the possible binding and activation states of the iLID system. Inactive

iLID is represented as a blue circle, active iLID is represented as a blue 10-pointed polygon, and SspB is

represented as a red circle. (B) Example plot of SspB concentration at the membrane over the course of a modeled light-stimulation experiment. Basal recruitment, max absolute recruitment, fold enrichment, and $t_{1/2}$ for dissociation are shown based on predicted species concentrations. (C) Illustration of cell-wide iLID stimulation. (D-G) Heatmaps depicting extent of basal recruitment (D), max absolute recruitment (E), max fold enrichment by recruitment (F), and $t_{1/2}$ for dissociation (G) across different iLID-to-SspB expression ratios generated using our ODE model. (H) Example confocal images showing distribution of SspB signal before (top-left panel) and after (top-right and bottom panels) global iLID stimulation using a 50 ms pulse of 445 nm light. Depicted cells express the Lyn11-iLID construct. Scale bar is 20 mm. (I) Plots of mean cytoplasmic SspB signal during confocal microscopy global stimulation experiments, with cells grouped based on estimated iLID-to-SspB ratio. The light pulse was applied between 1 and 2 seconds. Values are adjusted between 0 and 1 (From lowest to highest estimated iLID-to-SspB ratio: n=62 cells, n=54 cells, n=30 cells, n=55 cells). P<0.05 for $t_{1/2}$ for recovery between all groups except 2 and 3 (light blue and green curves, respectively). (J) For the experiment shown in H and I, predicted values were calculated from our ODE model using different iLID-to-SspB ratios and adjusted between 0 and 1. Total SspB concentration was 1.5 mM, and iLID concentrations were 50 nM (dark blue line), 1.5 mM (light blue line), 2 mM (green line), and 2.5 mM (yellow line).
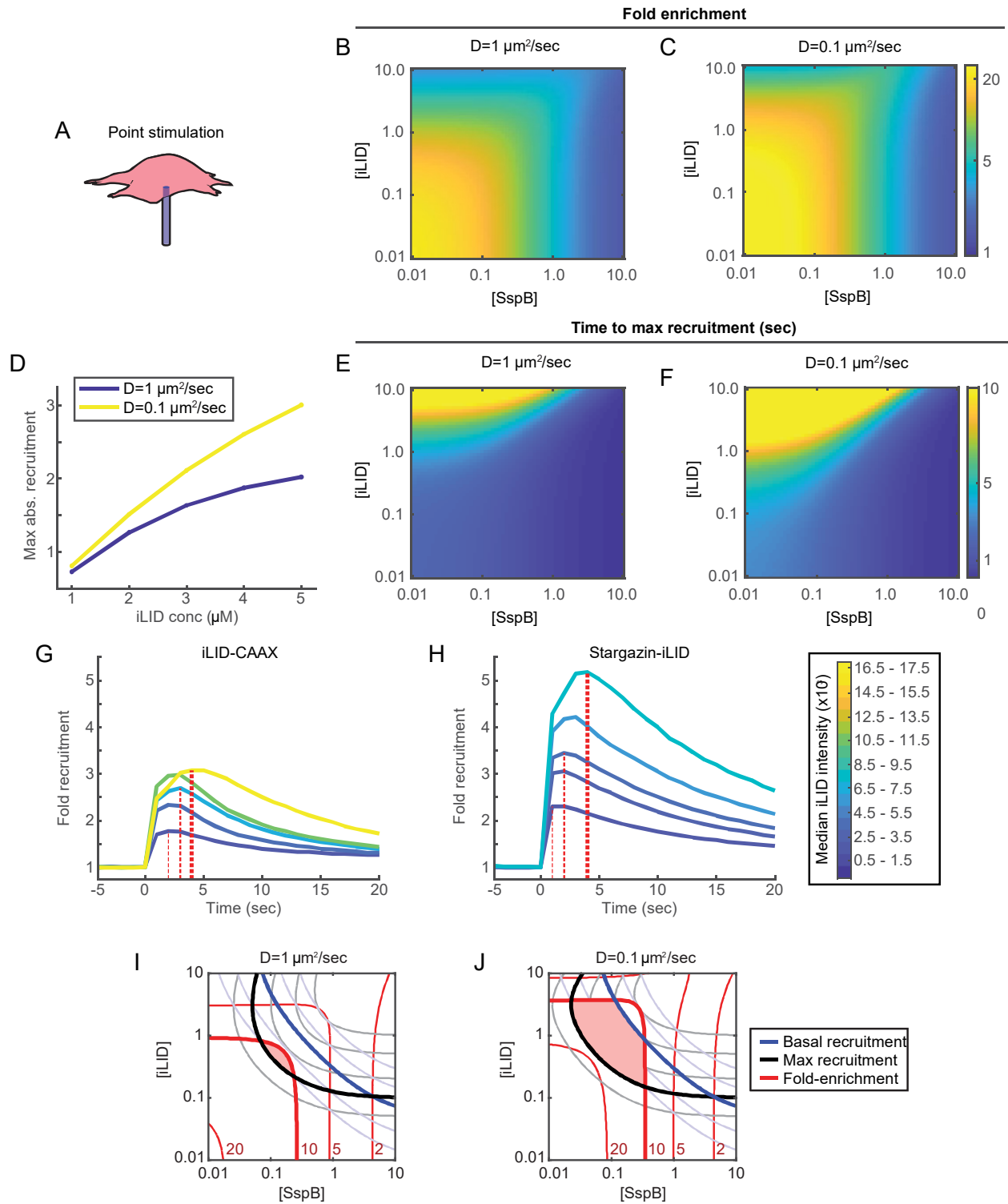
FIGURE 4

Figure 3.4. Overview of optimal expression regimes for subcellular recruitment.

(A) Illustration of subcellular iLID stimulation. (B-C) Heatmaps depicting max fold enrichment by recruitment at the stimulation site across different iLID-to-SspB expression ratios generated using our PDE model. Values were generated using a diffusion coefficient of 1 mm^2/sec (B) as an estimate for iLID-CAAX or 0.1 mm^2/sec (C) as an estimate for Stargazin-iLID. (D) Plots of predicted maximum absolute recruitment at varying iLID concentrations using a diffusion coefficient of 1 mm^2/sec (blue line) or 0.1 mm^2/sec (yellow line). The total concentration of SspB was 1 mM. (E-F) Heatmaps depicting time to max recruitment across different iLID-to-SspB expression ratios generated using our PDE model. Values were generated using a diffusion coefficient of 1 mm^2/sec (E) or 0.1 mm^2/sec (F). (G-H) Plots showing fold recruitment at the stimulation site over time for cells grouped by relative iLID expression, calculated from cells expressing iLID-CAAX (G) or Stargazin-iLID (H). The line colors correspond to median iLID fluorescence intensities. T_{max} values for the first, third, and fifth groups are shown by thin, medium, and thick vertical lines, respectively (For iLID-CAAX, from lowest to highest iLID-to-SspB ratio: n=14 cells, n=13 cells, n=20 cells, n=25 cells, n=7 cells. For Stargazin-iLID, from lowest to highest iLID-to-SspB ratio: n=20 cells, n=14 cells, n=26 cells, n=12 cells, n=7 cells). (I-J) Overlaid contour plots of basal recruitment (blue lines), max recruitment (black lines), and fold enrichment by recruitment (red lines). Lines indicating 50 nM basal recruitment, 100 nM max recruitment, and 10-fold enrichment are boldened, and fold enrichment contour lines are labeled in red along the X-axis. The shaded area indicates component expression ranges predicted to give optimal recruitment. Plots were generated using our PDE model with a diffusion coefficient of 1 mm^2/sec (I) or 0.1 mm^2/sec (J).
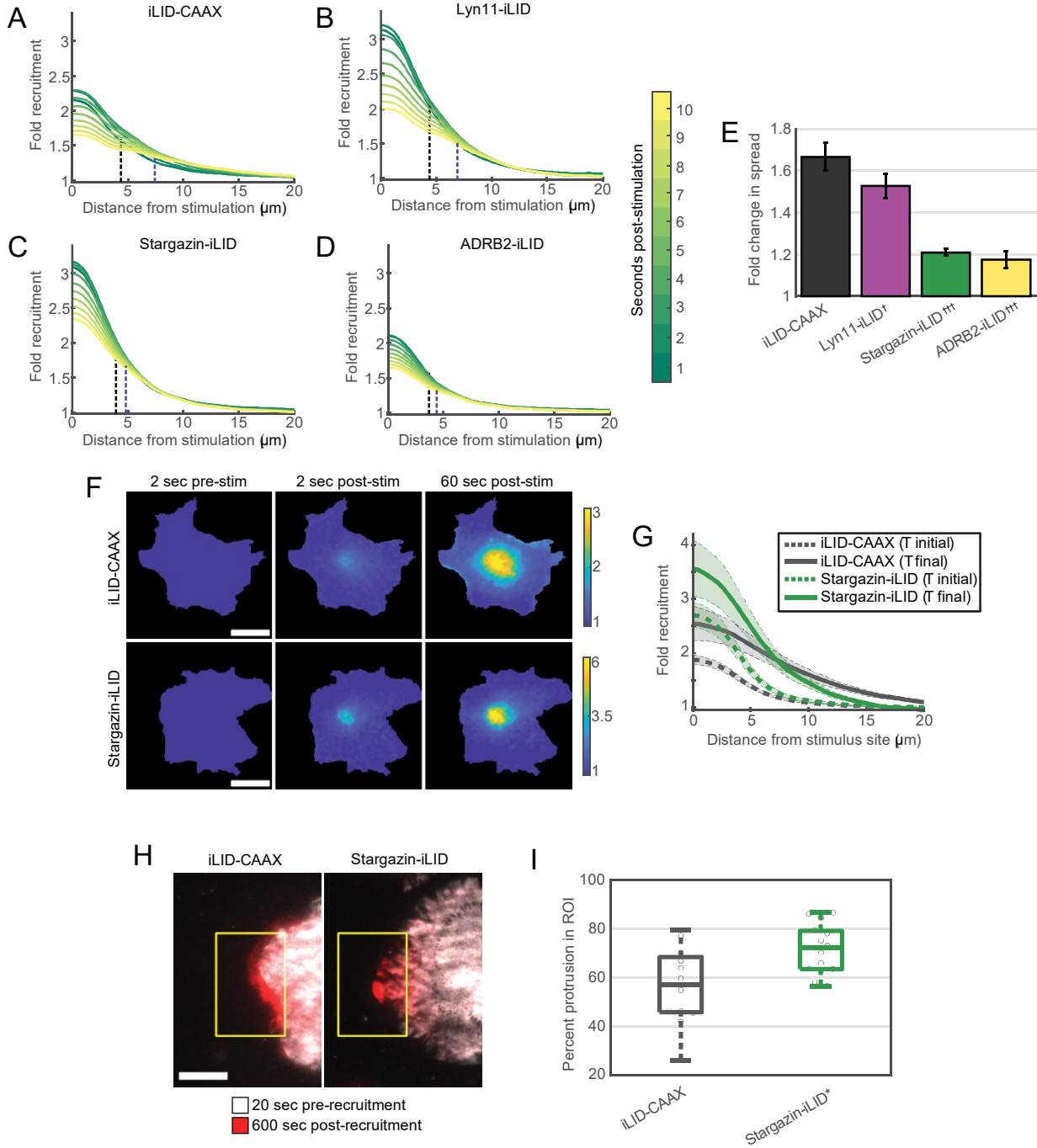
FIGURE 5

Figure 3.5. Spatial analysis of subcellular recruitment dynamics.

(A-D) Plots depicting mean SspB intensity as a function of radial distance from the stimulation site. Values

are normalized to pre-stimulation levels. Black and blue dotted lines indicate the distance of half-maximal

gradient signal 1 second and 10 seconds after stimulation, respectively (n=156 cells for iLID-CAAX, n=110 cells for Lyn11-iLID, n=138 cells for Stargazin-iLID, n=107 cells for ADRB2-iLD). (E) Bar graphs showing fold change in distance of the half-maximal gradient signal from 1 to 10 seconds post-stimulation, corresponding to the black and blue dotted lines in A-D. Error bars indicate ±S.E.M. †P<0.05 and †††P<0.001 for spread values below that of iLID-CAAX. P-values were calculated using the Mann-Whitney U test. (F) Example TIRF images of fold enrichment by recruitment during repeated point-stimulation for 1 minute using iLID-CAAX (top panels) or Stargazin-iLID (bottom panels). (G) Plots of mean SspB intensity as a function of radial distance from the stimulation site after repeated point-stimulation for 1 minute. Dotted lines show intensity gradients 1 second after the initial stimulation and solid lines show intensity gradients 1 second after the final stimulation. iLID-CAAX and Stargazin-iLID gradients are overlaid for comparison of magnitude and spatial confinement. Error bars indicate ±S.E.M (n=24 cells for iLID-CAAX, n=22 cells for Stargazin-iLID). (H) Example images depicting cell protrusions during Tiam1-SspB recruitment with iLID-CAAX (left panel) and Stargazin-iLID (right panel) over a 10 minute period. Cell edges before recruitment are shown in white and cell edges at the end of recruitment are shown in red. Yellow boxes indicate ROIs that were used for quantification. (I) Box plots of protrusion confinement after prolonged Tiam1-SspB recruitment. Values correspond to the percent of total protrusion area that was confined within the ROIs shown in H. Central line indicates the median, bottom and top box edges indicate 25$^{\text{th}}$ and 75$^{\text{th}}$ percentiles, and whiskers indicate most extreme data points not considering outliers. Black circles show distribution of single cell values (n=12 cells for iLID-CAAX, n=15 for Stargazin-iLID). *P<0.02 for values above that of iLID-CAAX. P-values were calculated using the Mann-Whitney U test.

TABLE 1

Table 1. Summary of recommendations for membrane recruitment using iLID

Experimental goal	Optimized for	Recommended construct	Recommended expression conditions
Global recruitment	Low background	Lyn11-iLID or Stargazin-iLID	Low expression levels
			Equivalent component expression levels
	Strong recruitment	Lyn11-iLID or Stargazin-iLID	Intermediate expression levels
			Equivalent component expression levels
Subcellular recruitment	Low background	Stargazin-iLID	Intermediate iLID expression levels
			High iLID-to-SspB ratio
	Strong recruitment	Stargazin-iLID	High iLID expression levels
			High iLID-to-SspB ratio

Table 3.1. Summary of recommendations for membrane recruitment using iLID.
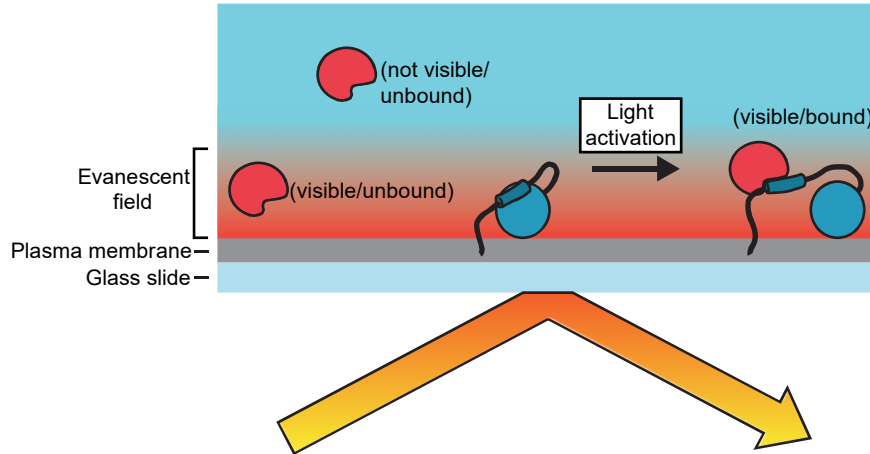
3.13 Supplemental Information

Figure S1

Figure S3.1. Molecule-scale illustration showing how SspB recruitment is visualized via TIRF microscopy

SspB molecules are represented as red circles and iLID molecules are represented as blue circles. When incident light hits the sample at a critical angle, total internal reflection creates an evanescent field that illuminates fluorescent proteins within 100-200 nm of the basal plasma membrane. Prior to stimulation, most SspB molecules are unbound from iLID and not visible by TIRF. However, a small fraction of cytoplasmic SspB is proximal to the membrane and visible. After stimulation, SspB molecules that bind to activated iLID are recruited into the field of view at high concentrations.
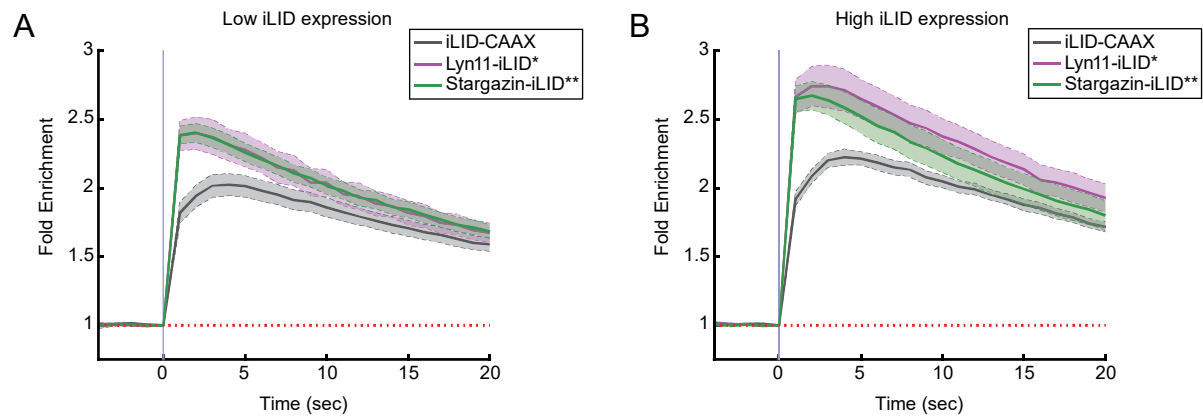
Figure S2

Figure S3.2. Plots of fold change in SspB recruitment upon global illumination

Plots showing fold change in SspB membrane recruitment after global illumination with 445 nm light using iLID-CAAX, Lyn11-iLID, and Stargazin-iLID. Cell were organized into two groups based on defined ranges of mTurquoise fluorescence to allow comparison of cells with equivalent component expression levels. ADRB2-iLID was not included because the range of expression was much lower for this construct. (A) Mean fold recruitment for cells in the lower range of iLID expression. Error bars indicate ±S.E.M (n=16 cells for iLID-CAAX, n=7 cells for Lyn11-iLID, n=21 cells for Stargazin-iLID). *P<0.05 for maximum recruitment values above that of iLID-CAAX. **P<0.002 for maximum recruitment values above that of iLID-CAAX. P-values were calculated using the Mann-Whitney U test. (B) Mean fold recruitment for cells in the higher range of iLID expression. Error bars indicate ±S.E.M (n=11 cells for iLID-CAAX, n=9 cells for Lyn11-iLID, n=13 cells for Stargazin-iLID). *P<0.05 for maximum recruitment values above that of iLID-CAAX. **P<0.002 for maximum recruitment values above that of iLID-CAAX. P-values were calculated using the Mann-Whitney U test.
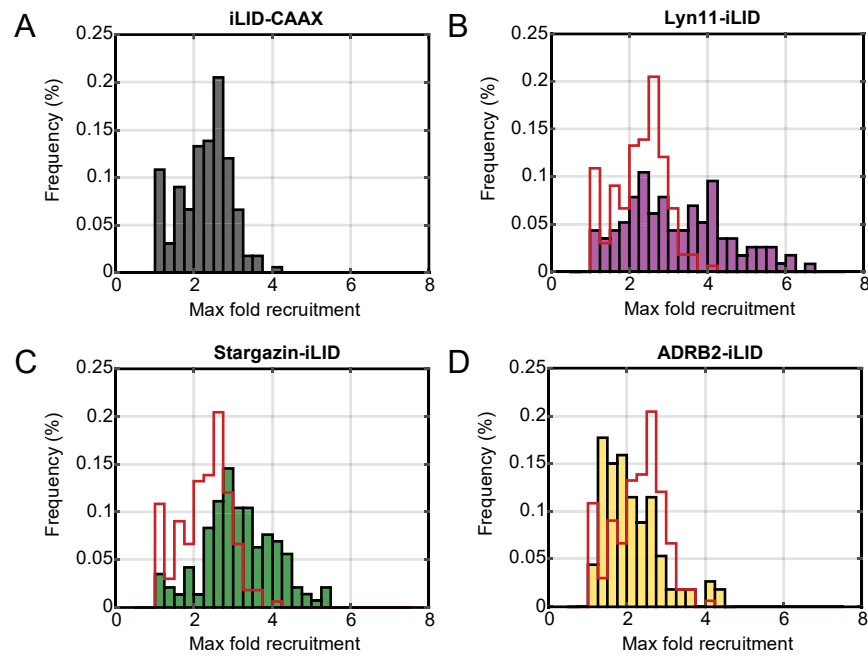
Figure S3

Figure S3.3. Histograms of maximum fold change in recruitment in individual cells from point-recruitment experiments

Histrograms show single cell data for iLID-CAAX (A), Lyn11-iLID (B), Stargazin-iLID (C), and ADRB2-iLID (D). Bin edges and widths were constant for all constructs. In B-D, iLID-CAAX data is overlaid as red stairs for easy comparison.

Figure S4

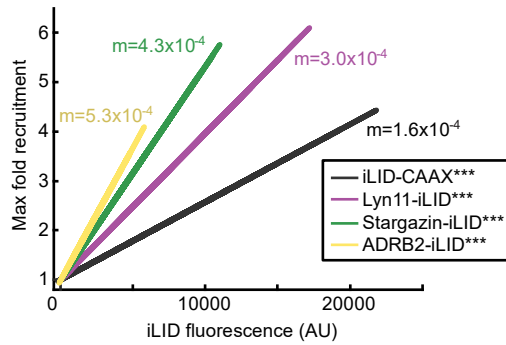**Figure S3.4. Fit lines from Figures 2E-2H are overlaid with slope values indicated**

The slope of the correlation is substantially steeper for N-terminal versus C-terminal anchors, and also increases according to anchor size. ***$P<0.001$ for best fit slope values that are significantly different from slope values of all other conditions. P-values were calculated using a permutation test with 10,000 random permutations.

Figure S5
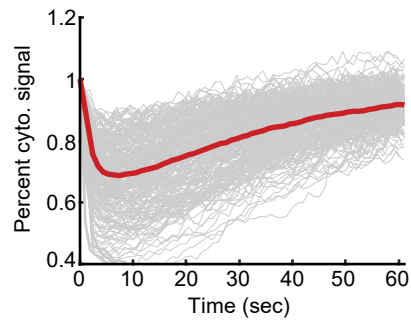
Figure S3.5. Plots of cytoplasmic SspB signal from confocal imaging

Plots of cytoplasmic SspB intensity in Lyn11-iLID expressing cells during confocal microscopy global stimulation experiments. Single cell traces are shown in gray, and mean trace of all cells is shown in red. The light pulse was applied between 1 and 2 seconds. Values are normalized to pre-stimulus levels such that recruitment and recovery are depicted as fractions of total SspB signal.

Figure S6
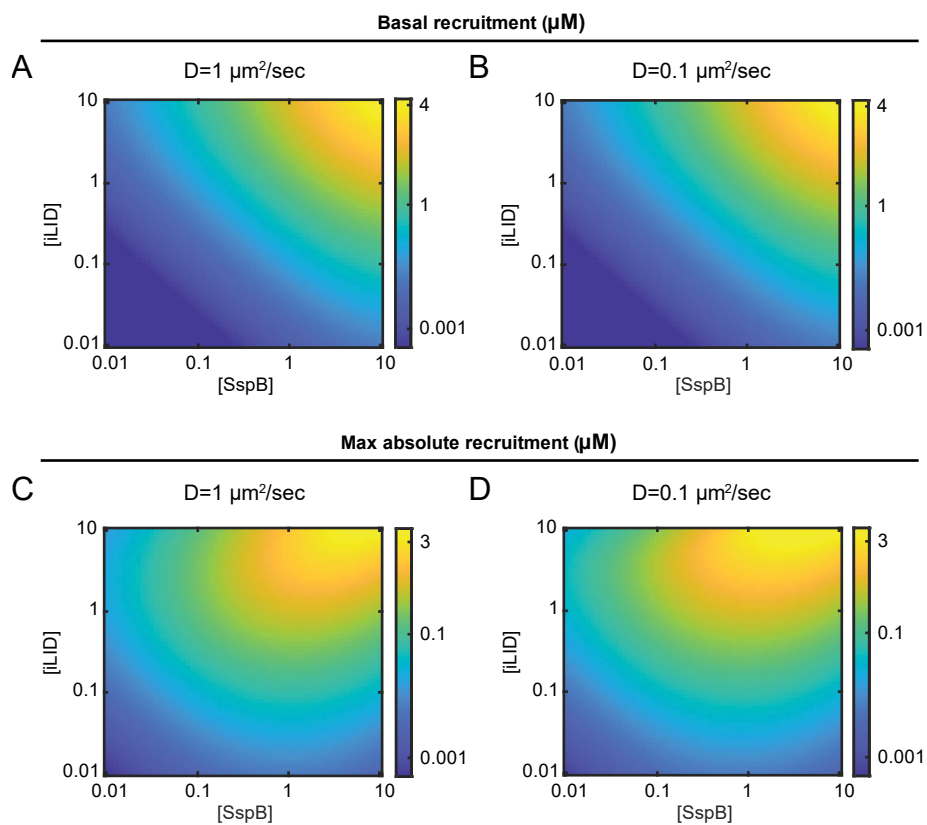
Figure S3.6. Recruitment heatmaps from PDE model predictions

(A-B) Heatmaps of basal recruitment at iLID and SspB concentrations ranging from 10 nM to 10 mM, using a diffusion coefficient of 1 mm^2/sec (A) or 0.1 mm^2/sec (B). Heatmaps are identical with both diffusion rates, since basal recruitment occurs uniformly throughout the membrane. (C-D) Heatmaps of max absolute recruitment at iLID and SspB concentrations ranging from 10 nM to 10 mM, using a diffusion coefficient of 1 mm^2/sec (C) or 0.1 mm^2/sec (D). Note the asymmetry in absolute recruitment with increasing component concentrations, which becomes more exaggerated with a smaller diffusion coefficient.
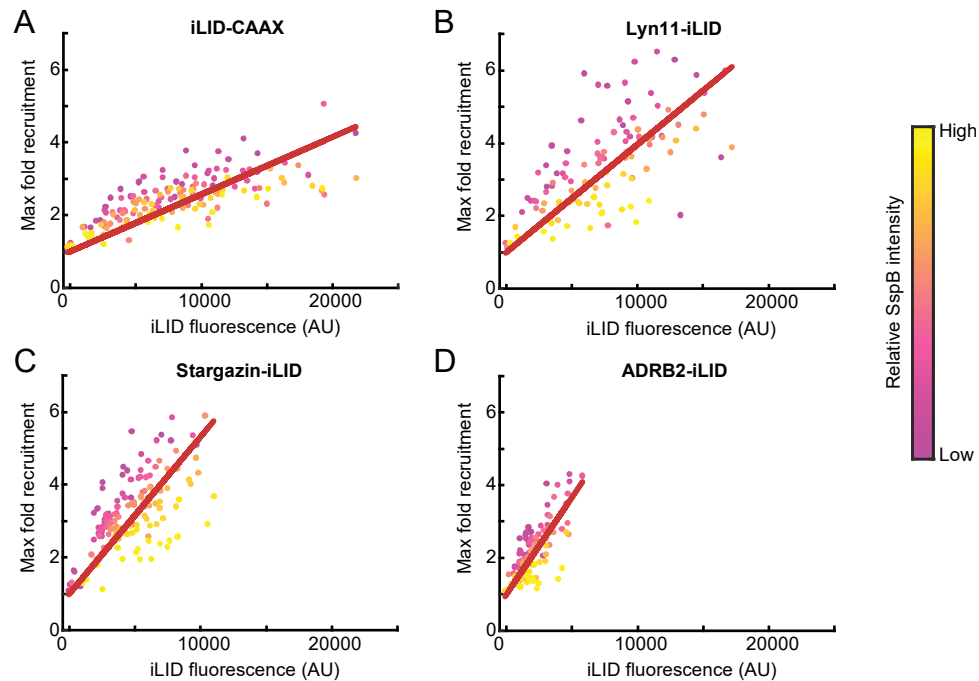
Figure S3.7. Scatter plots of iLID fluorescence vs max fold recruitment with basal SspB intensity

Scatter plots of iLID fluorescence vs max fold recruitment after point-stimulation for iLID-CAAX (A), Lyn11-iLID (B), Stargazin-iLID (C), and ADRB2-iLID (D), as shown in Figures 2E-2H. Single cell data points are pseudocolored according to basal SspB intensity, with low SspB intensity in pink and high SspB intensity in yellow. Pseudocolor ranges are set according to the minimum and maximum basal SspB intensity for each condition.

Figure S8
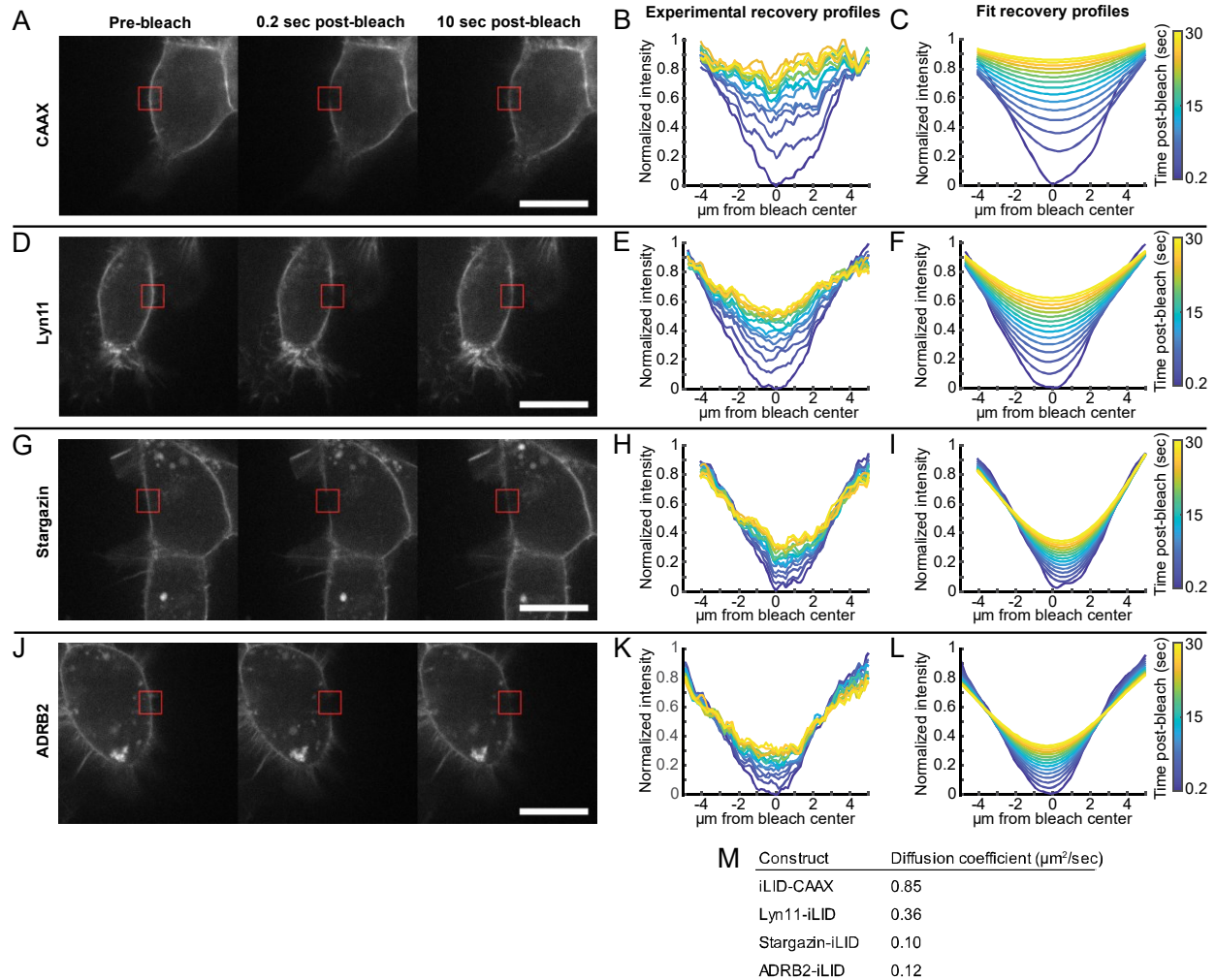
Figure S3.8. Example images and quantification of iLID diffusion via FRAP

mTurquoise2-labelled iLID was photobleached within a 5 mm^2 region of the cell membrane, and fluorescence recovery was calculated over time. (A, D, G, J) Example images of iLID fluorescence before (left panels), 0.2 seconds after (middle panels), and 10 seconds after (right panels) photobleaching with high-intensity 488 nm light. Bleached regions are indicated by red boxes. (B, E, H, K) iLID fluorescence recovery profiles for iLID-CAAX (B), Lyn11-iLID (E), Stargazin-iLID (H), and ADRB2-iLID (K) calculated as a function of distance from the bleach center. (C, F, I, L) Modeled iLID recovery profiles for iLID-CAAX (C), Lyn11-iLID (F), Stargazin-iLID (I), and ADRB2-iLID (L) generated by fitting a PDE

diffusion model to profiles in (B, E, H, K). (M) Diffusion coefficients estimated by fitting the PDE diffusion

models.
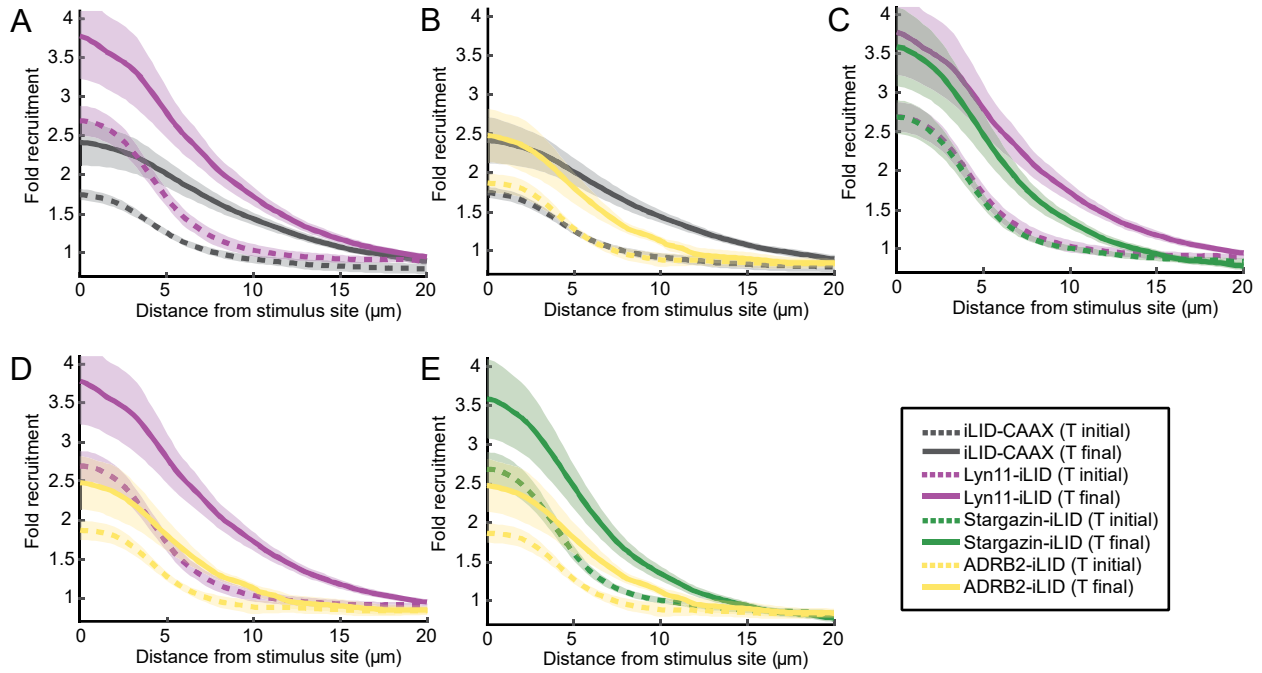
Figure S3.9. Spatial SspB intensity gradients from multi-stimulation experiments

Dotted lines show intensity gradients 1 second after the initial stimulation and solid lines show intensity gradients 1 second after the final stimulation. Error bars indicate ±S.E.M. (n=25 cells for iLID-CAAX, n=33 for Lyn11-iLID, n=22 cells for Stargazin-iLID, n=12 for ADRB2-iLID). Plots show direct comparison of SspB intensity gradients for iLID-CAAX and Lyn11-iLID (A), iLID-CAAX and ADRB2-iLID (B), Lyn11-iLID and Stargazin-iLID (C), Lyn11-iLID and ADRB2-iLID (D), and Stargazin-iLID and ADRB2-iLID (E).

Figure S10
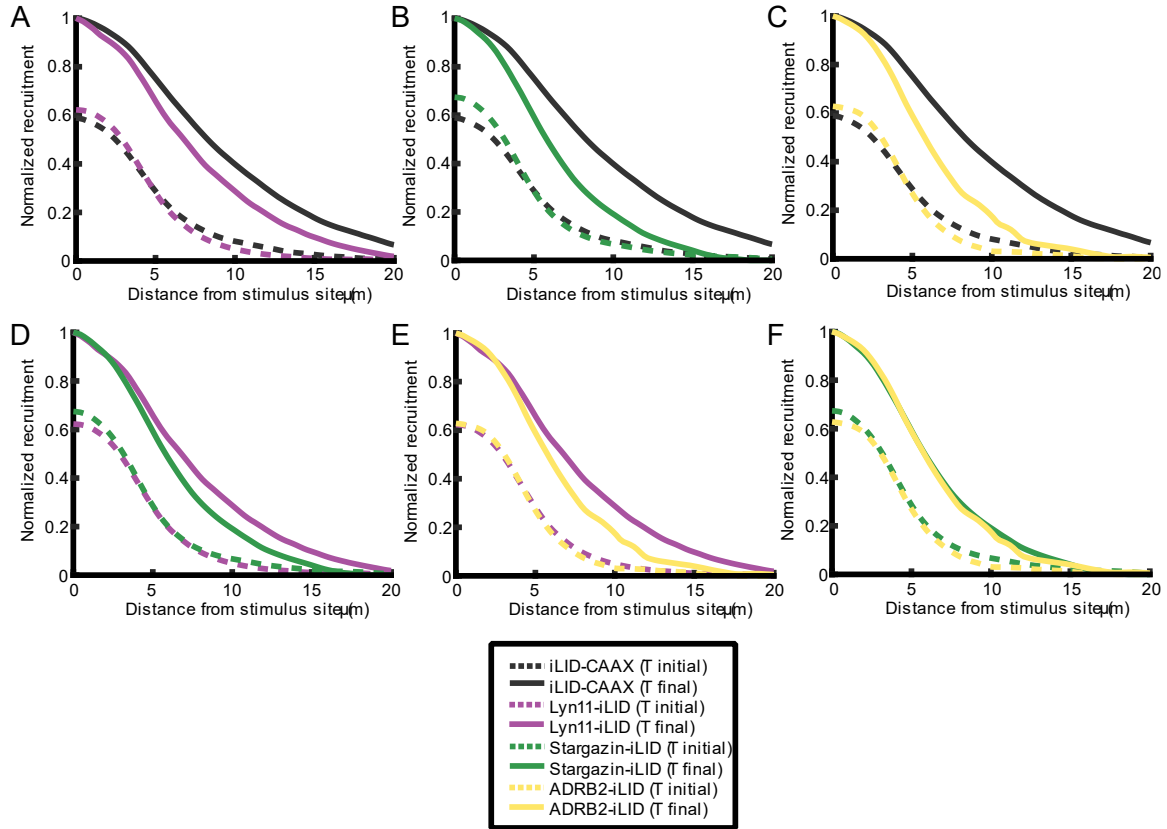
Figure S3.10. Normalized spatial SspB intensity gradients from multi-stimulation experiments as shown in Figure S8

Values are adjusted to a scale from 0 to 1 to allow easier comparison of the spatial extent of signal spreading for each construct. Dotted lines show intensity gradients 1 second after the initial stimulation and solid lines show intensity gradients 1 second after the final stimulation. Plots show direct comparison of normalized SspB intensity gradients for iLID-CAAX and Lyn11-iLID (A), iLID-CAAX and Stargazin-iLID (B), iLID-CAAX and ADRB2-iLID (C), Lyn11-iLID and Stargazin-iLID (D), Lyn11-iLID and ADRB2-iLID (E), and Stargazin-iLID and ADRB2-iLID (F).

Figure S11
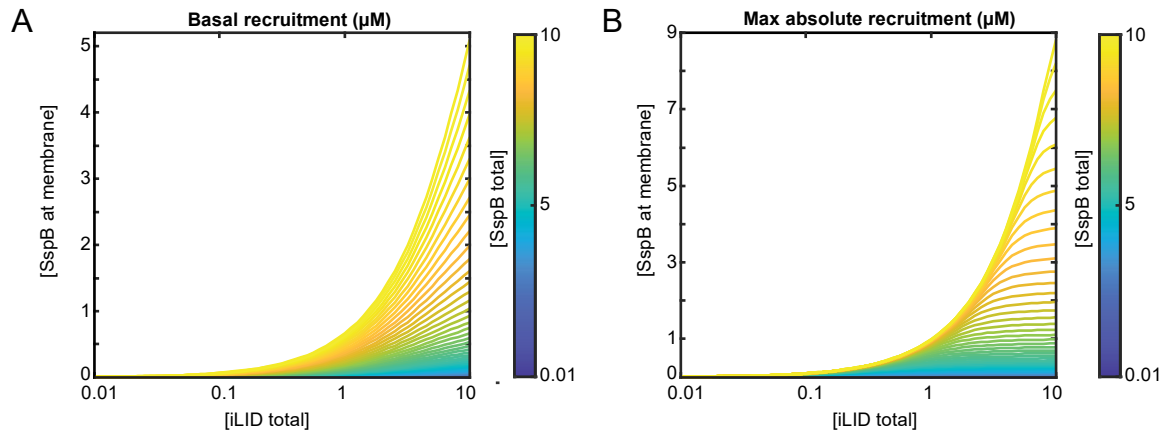
Figure S3.11. Visualization of ODE recruitment heatmaps as line plots

Plots of basal recruitment (A) and max absolute recruitment (B) as a function of iLID concentration, and generated across a range of SspB concentrations (depicted as different line colors). Component concentrations range from 10 nM to 10 mM. Both features show steep increases, especially at mid-range to high component concentrations.

Chapter 4

Compatible tools to simultaneously perturb and monitor Rho GTPase signaling with light

Dean E. Natwick[1] and Sean R. Collins[1*]

[1]Department of Microbiology and Molecular Genetics, University of California, Davis, Davis, CA 95616, United States

4.1 Preface

This chapter presents a novel red-shifted RhoA FRET biosensor that, along with a recently developed Cdc42 FRET biosensor, is compatible with blue light-activated optogenetic systems. These biosensors are combined with iLID-based Rho GTPase activation in a neutrophil model, PLB-985. This work demonstrates the ability to directly measure optogenetic Rho GTPase activation in PLB-985 cells and applies this approach to the identification of a novel RhoA-to-Cdc42 crosstalk connection. Furthermore, precise light patterning is used to demonstrate subcellular Rho GTPase activation, which is sufficient to drive cell migration using light.

4.2 Author contributions

D.E.N. and S.R.C. conceived and designed the experiments. D.E.N. generated all constructs and cell lines and performed all experiments and data analyses with input from S.R.C.

4.3 Abstract

Neutrophils use chemotaxis, the directed migration along chemical gradients, to navigate tissues to fight infection. Migration requires the generation of intracellular polarity and coordination between distinct cell front and rear domains. This is largely regulated through Rho family GTPases, which activate diverse signaling pathways at different regions within the cell. Cdc42 and RhoA are especially important organizers of front and rear activities, respectively. While signaling crosstalk between Rho GTPases has long been theorized to contribute to the spatial organization of front and rear domains, we have lacked the molecular tools necessary for measuring signaling crosstalk directly. Here, we pair an optogenetic strategy for light-controlled Rho GTPase activation with spectrally compatible FRET biosensors for Cdc42 and RhoA. Using these tools in a neutrophil model cell line, PLB-985, we demonstrate the ability to measure both direct Rho GTPase activation as well as a novel RhoA-to-Cdc42 crosstalk connection. Furthermore, we demonstrate subcellular Rho GTPase activation and show that local Cdc42 and RhoA activity is sufficient to bias neutrophil migration.

4.4 Results

4.4.1 Red-shifted FRET biosensors for Cdc42 and RhoA activity in live cells

Recently, we developed a slow-diffusing version of the iLID system (Stargazin-iLID) that affords even higher spatial control over signaling proteins compared to the original iLID-CAAX version[1]. This tool was used to recruit a Rac GEF to the plasma membrane using subcellular light stimulation and elicit highly-localized membrane protrusion and ruffling. However, using this optogenetic tool to directly measure Rho GTPase signaling patterns requires spectrally compatible live cell biosensors. To this end, we built single-chain red-shifted FRET biosensors for Cdc42 and RhoA. Using the design strategy for the Raichu Rho GTPase FRET sensors from the Matsuda lab at Kyoto University, we swapped the original cyan and yellow fluorescent proteins for tdTomato and tdKatushka2, respectively, and term these TomKat biosensors[2,3]. The Cdc42 TomKat sensor was previously characterized and used to study signal

processing downstream of optogenetic receptor activation in PLB-985 cells[4]. To validate the Cdc42 and

RhoA TomKat sensors in parallel, we first measured the global average FRET response of cells stably

expressing each sensor upon stimulation with the chemoattractant formyl peptide, N-formyl-methionyl-

leucyl-phenylalanine (fMLF). Previous studies showed that total Cdc42 activity increases while total

RhoA activity decreases upon fMLF stimulation[5]. In agreement with this, upon addition of fMLF, we

observed a rapid increase in average FRET ratio with the Cdc42 biosensor and a rapid decrease in average

FRET ratio with the RhoA biosensor (Figure 1A and 1B). The response kinetics measured with both

biosensors also aligned with previous data. We further validated the sensors by measuring the spatial

FRET activity pattern in migrating PLB-985 cells. The Cdc42 TomKat sensor showed a steep front-

oriented activity pattern that peaked at the leading edge (Figure 1C). Meanwhile, the RhoA TomKat

sensor reported low RhoA activity at the cell leading edge, which gradually increased within the cell body

and rear (Figure 1D). Both spatial patterns were very similar to the activity patterns measured with the

original Raichu sensors in PLB-985 cells[5]. Together, these experiments confirm that the Cdc42 and RhoA

TomKat sensors faithfully report on the activities of their respective GTPases with high spatial and

temporal resolution.

4.4.2 Global light stimulation reveals kinetics of Rho GTPase activation and a novel signaling crosstalk connection

We wanted to test whether the Stargazin-iLID system and TomKat sensors could be used to

simultaneously activate and measure Rho GTPase signaling in PLB-985 cells. We generated stable PLB-

985 lines co-expressing Stargazin-iLID with either ITSN-mCitrine-SspB and the Cdc42 TomKat sensor

or ARHGEF1-mCitrine-SspB and the RhoA TomKat sensor. ITSN and ARHGEF1 are RhoGEFs that

strongly activate Cdc42 and RhoA, respectively, but not other Rho GTPases. We then performed time

lapse FRET imaging while applying repeated 40 ms global pulses of 445 nm light between each FRET

acquisition to a population of undifferentiated PLB-985 cells for 2 minutes. Undifferentiated cells were

used to simplify analysis, as undifferentiated cells were non-motile and had smaller stochastic fluctuations

in FRET activity. For both biosensors, the total mean FRET ratio increased rapidly upon 445 nm light

stimulation, peaking within ~15 seconds and remaining elevated throughout the entire stimulus period

(Figure 2A and 2B, dark magenta line). These results confirmed the compatibility of the optogenetic

system with the biosensors. Furthermore, they served as additional validation of the biosensors as well as

our ability to activate Rho GTPases using iLID.

We next wanted to determine whether this experimental approach could be used to measure

crosstalk signaling kinetics directly. Therefore, we generated a stable PLB-985 line co-expressing

Stargazin-iLID with ARHGEF1-mCitrine-SspB and the Cdc42 TomKat sensor. This would enable

measurement of Cdc42 activity in response to acute RhoA activation. It is important to note that, because

the light stimulation is global, this assay can only reveal dominant and local signaling crosstalk.

Performing the same time lapse FRET experiment as above in undifferentiated cells, we found a decrease

in Cdc42 activity in response to increased RhoA activity (Figure 2C, dark green line). The onset of Cdc42

inactivation began ~12 seconds after the first 445 nm stimulation, a delay that is in alignment with the

time required for RhoA activity to begin to peak. To determine whether this signaling response was

dependent on RhoA signaling through Rho-associated protein kinse (ROCK), a primary effector signaling

protein, we repeated the experiment in cells treated with the ROCK inhibitor, Y27632. Indeed, cells

treated with Y27632 showed no change in Cdc42 activity, supporting the idea that RhoA negatively

regulates Cdc42 activity through downstream signaling via ROCK (Figure 2C, light green line and 2D).

Importantly, Y27632 did not affect the magnitude or kinetics of direct RhoA activation (Figure 2B, light

magenta line).

4.4.3 Subcellular light stimulation is sufficient to bias cell migration

A major benefit of our optogenetic strategy is the potential for spatial control over signaling. To

test whether we could pattern subcellular Rho GTPase activities, we performed an automated cell center

stimulation TIRF imaging assay with differentiated PLB-985 cells expressing Stargazin-iLID, ITSN-

mCitrine-SspB, and the Cdc42 TomKat sensor. Time lapse TIRF FRET imaging was performed while

repeated 25 ms pulses of 445 nm light were applied to a ~2x2 µm region of the cell centroid using LED

light guided through a digital micromirror device. At the end of each time course experiment, a single

78

TIRF image with 514 nm light was acquired to visualize the recruitment gradient of the ITSN-mCitrine-SspB construct. Cdc42 activity began increasing at the cell center immediately after light stimulation and continued to increase locally until an apparent maximum activation threshold was reached after roughly 30 seconds of repeated stimulation (Figure 3A). Importantly, Cdc42 activity did not increase substantially at the cell periphery where light stimulation was not applied. Indeed, the shape of the FRET-change activity gradient was remarkably similar the shape of the ITSN-mCitrine-SspB recruitment gradient (Figure 3B).

Finally, we asked whether we could bias the migration of differentiated PLB-985 cells using local Rho GTPase activation at the cell edge. We performed an automated TIRF FRET imaging experiment in which we performed time lapse TIRF imaging to track individual cells and repeatedly stimulated a small region of the cell edge for two minutes. In cells expressing ITSN-mCitrine-SspB, Cdc42 activation at the cell edge caused cells to gradually turn and migrate in the direction of the light pulse (Figure 3C, top row). In contrast, in cells expressing ARHGEF1-mCitrine-SspB, activation of RhoA at the cell edge caused gradual turning and migration away from the light pulse (Figure 3C, bottom row). These results align with similar experiments performed in RAW 264.7 cells, a macrophage cell line[6,7]. It is noteworthy that, in both cases, cells maintained and reoriented their existing polarity axis, rather than repolarizing in response to GTPase activation. This recapitulates a well-characterized tendency for neutrophils to steer by performing U-turns during chemotaxis[8]. These results demonstrate that local activities of Cdc42 and RhoA are both sufficient to orient cell polarity and drive migration by initiating cell turning.

4.5 Methods

4.5.1 Plasmids

All iLID and SspB constructs were cloned into lentiviral expression plasmids. The Stargazin-iLID plasmid was generated as previously outlined[1]. The ITSN-mCitrine-SspB and ARHGEF1-mCitrine-SspB plasmids were generated by PCR amplifying the DH domain of ITSN1 (residues 1,229-1,449), the

DH domain of ARHGEF1 (residues 382-645), and an mCitrine-SspB fusion. DNA fragments were integrated into a linearized 2nd generation lentiviral expression plasmid via Gibson Assembly. The TomKat sensors were cloned into plasmids for stable expression via the piggybac transposase system. The Cdc42 TomKat sensor was generated as previously outlined[4]. The RhoA TomKat sensor was generated by restriction digesting the Cdc42 TomKat sensor plasmid to remove the PAK-EVlinker-Cdc42 region but leaving td-Tomato and td-Katushka2 on either end. A PKN1-EVlinker-RhoA fusion was PCR amplified from the Matsuda lab's RhoA Raichu sensor. Finally, the fusion was cloned into the digested Cdc42 TomKat plasmid via Gibson Assembly.

4.5.2 Cell culture

PLB-985 cells were cultured in RPMI 1640 media (Gibco) supplemented with 10% FBS and 1% penicillin and streptomycin (RPMI complete media). Cells were differentiated into a neutrophil-like state by culturing 2×10^5 cells per ml in RPMI complete media with 1.3% DMSO and 2% Nutridoma-CS (Roche) for 6 days. HEK293T cells were cultured in high glucose DMEM medium with sodium bicarbonate (Sigma-Aldrich) and supplemented with 10% FBS, 1% penicillin and streptomycin, and 1% GlutaMax (Thermo Fisher). All cell lines were maintained in a humidified incubator at 37 °C and 5% atmospheric CO2.

4.5.3 Cell line construction.

Cdc42 and RhoA TomKat sensors were stably expressed in PLB-985 cells by co-electroporating each plasmid at a 1:1 ratio with a piggybac transposase expression plasmid. Electroporation was performed with the Neon electroporation system (Sigma-Aldrich) according to the manufacturer recommendations for 100 μl electroporation volumes. Briefly, 2×10^6 cells were resuspended in 100 μL of Buffer R, 5 μg of each plasmid were added to the cells, and 1 35-ms electrical pulse at 1350 V was applied. Following this, cells were immediately transferred to RPMI complete media, then antibiotic selection was started 24 hours later. Stargazin-iLID and all SspB constructs were stably expressed in PLB-985 cells via subsequent rounds of lentivirus transduction and antibiotic selection.

4.5.4 Microscopy

All microscopy experiments were performed on a Nikon Eclipse Ti-E inverted fluorescence microscope with dual Andor Zyla 4.2 sCMOS cameras, a Mightex Polygon DMD pattern illuminator, and 37° C temperature-controlled chamber. FRET donor and acceptor channels were simultaneously acquired on separate cameras using a Cairn TwinCam LS image splitter. The microscope was controlled using a MATLAB interface for Micromanager to automate optogenetic stimulation and image acquisition.

To image TomKat biosensor dynamics during fMLF stimulation, 5×10^5 differentiated cells were plated in 100 μL of modified L-15 media on 96-well glass-bottom plates (Cellvis) pre-treated with 200 μg/mL poly-D-lysine (Sigma-Aldrich). fMLF was prepared at 200 μM in modified L-15 media and warmed to 37° C. Time lapse TomKat FRET imaging was performed via epifluorescence illumination using a 10x objective. Images were acquired every 3 seconds for 42 seconds, and 100 μL of fMLF was a added to the cells between the third and fourth acquisitions. To image TomKat biosensor spatial activity gradients, 3×10^4 differentiated cells were plated on 96-well glass-bottom plates under agarose as described previously[9]. TomKat FRET imaging was performed via TIRF microscopy using a 60x 1.49 NA Apo TIRF oil immersion objective. Images were acquired every 3 seconds for 60 seconds.

For global iLID stimulation and FRET imaging experiments, 5×10^5 undifferentiated cells were plated in 100 μL of modified L-15 media on 96-well glass-bottom plates pre-treated with 200 μg/mL poly-D-lysine. Time lapse TomKat FRET imaging was performed via epifluorescence illumination using a 10x objective. Images were acquired every 3 seconds for 135 seconds. Global 445 nm light stimulation was applied by acquiring an epifluorescence CFP image with a 40 ms exposure time. 445 nm light was applied between FRET image acquisitions beginning after the fifth acquisition and continuing until the end of the time course.

For cell center stimulation and FRET imaging experiments, differentiated cells were plated under agarose as described above. Time lapse TomKat FRET imaging was performed via TIRF microscopy using a 60x 1.49 NA Apo TIRF oil immersion objective. Cell detection, optogenetic stimulation, and imaging were carried out using custom automated software. Cells were imaged in parallel by iterating

through different imaging windows within wells. At each window, a cell was selected and automatically tracked by centering the imaging field on the cell centroid prior to each FRET acquisition. Images were acquired every 3 seconds for 129 seconds. Beginning after the 4th acquisition, a ~2 μm^2 region of the cell center was illuminated between FRET acquisitions for 25 ms with 445 nm laser light patterned through the Polygon DMD. Cell edge stimulation experiments for driving analysis were performed using a similar strategy. However, instead of centering on the cell centroid, a predefined point on the cell periphery was defined as the stimulation target site.

4.5.5 Image analysis

All post-processing steps and image analyses were performed using MATLAB. For all images, corrections were first applied to account for artifacts from camera dark-state noise, differences in camera chip sensitivity, and dust in the light path. All TomKat FRET image pairs were registered using a custom coordinate-mapping strategy, then cropped to equal sizes[5]. Additionally, a systematic top-to-bottom FRET gradient was observed in all TomKat ratio images. This was corrected by dividing each FRET ratio image by a smoothed, empirically-generated 2D ratio correction image as described[4].

To calculate TomKat FRET responses to fMLF stimulation, the artifact correction and image registration steps were carried out as described above. For each cell, a global average FRET value for each time point was calculated by dividing the mean FRET acceptor value within cell pixels by the corresponding mean FRET donor value. A final FRET response curve was calculated by averaging values across all cells. The same strategy was used to calculate FRET changes in response to global optogenetic stimulation.

To determine the spatial activity gradients of the TomKat sensors, only frames in which cells were polarized and moving were included in analysis. First, artifact correction and image registration steps were carried out as described above. Next, high-resolution FRET ratio images were generated using the methodology described[5]. Briefly, for both FRET images, local background subtraction was performed, then a summed image was generated. Using the summed image, cell edges were enhanced using unsharp masking, then intensity-based cell segmentation was performed to generate a cell mask. For individual

FRET images, smoothing was applied to reduce pixel noise, then the cell mask was applied to isolate cell pixels. FRET ratios were calculated by dividing the segmented FRET acceptor image by the segmented FRET donor image on a pixel-by-pixel basis, then dividing by the 2D ratio correction image in the same way. For each cell, the cell front was identified by subtracting cell masks, then pixels within the mask were binned according to their distance from the front region. Average FRET values were calculated for each bin in each frame. Final FRET activity gradients for each cell were calculated by taking the mean across all frames. A final FRET activity gradient for each biosensor was calculated by taking the mean across all cells.

To calculate FRET changes during subcellular optogenetic stimulation experiments, the strategies described above for generating high-resolution FRET images were used. Pixels within cell masks were binned according to their distance from the stimulation site, which was determined empirically. For each cell, the average FRET value in each bin was calculated from frame to frame. The mean across all cells was calculated to determine final FRET change gradients.

4.6 Acknowledgements

4.7 References

(1)   Natwick, D. E., Collins, S. R. (2021) Optimized ILID Membrane Anchors for Local Optogenetic Protein Recruitment. *ACS Synth. Biol. 10* (5), 1009–1023.

https://doi.org/10.1021/acssynbio.0c00511.

(2)   Itoh, R. E., Kurokawa, K., Ohba, Y., Yoshizaki, H., Mochizuki, N., Matsuda, M. (2002) Activation of Rac and Cdc42 Video Imaged by Fluorescent Resonance Energy Transfer-Based Single-Molecule Probes in the Membrane of Living Cells. *Mol. Cell. Biol.* *22* (18), 6582–6591. https://doi.org/10.1128/MCB.22.18.6582.

(3)   Yoshizaki, H., Ohba, Y., Kurokawa, K., Itoh, R. E., Nakamura, T., Mochizuki, N., Nagashima, K., Matsuda, M. (2003) Activity of Rho-Family GTPases during Cell Division as Visualized with FRET-Based Probes. *J. Cell Biol.* *162* (2), 223–232. https://doi.org/10.1083/jcb.200212049.

(4)   Bell, G. R. R., Rincón, E., Akdoğan, E., Collins, S. R. (2021) Optogenetic Control of Receptors Reveals Distinct Roles for Actin- and Cdc42-Dependent Negative Signals in Chemotactic Signal Processing. *bioRxiv* 1–43.

(5)   Yang, H. W., Collins, S. R., Meyer, T. (2016) Locally Excitable Cdc42 Signals Steer Cells during Chemotaxis. *Nat. Cell Biol.* *18* (2), 191–201. https://doi.org/10.1038/ncb3292.

(6)   O'Neill, P. R., Kalyanaraman, V., Gautam, N. (2016) Subcellular Optogenetic Activation of Cdc42 Controls Local and Distal Signaling to Drive Immune Cell Migration. *Mol. Biol. Cell* *27* (9), 1442–1450. https://doi.org/10.1091/mbc.E15-12-0832.

(7)   O'Neill, P. R., Castillo-Badillo, J. A., Meshik, X., Kalyanaraman, V., Melgarejo, K., Gautam, N. (2018) Membrane Flow Drives an Adhesion-Independent Amoeboid Cell Migration Mode. *Dev. Cell* *46* (1), 9-22.e4. https://doi.org/10.1016/j.devcel.2018.05.029.

(8)   Zigmond, S. H., Levitsky, H. I., Kreel, B. J. (1981) Cell Polarity : An Examination of Its Behavioral Expression and Its Consequences for Polymorphonuclear Leukocyte Chemotaxis. *J. Cell Biol.* *89*, 585–592.

(9)   Bell, G. R. R., Natwick, D. E., Collins, S. R. (2018) Parallel High-Resolution Imaging of Leukocyte Chemotaxis under Agarose with Rho-Family GTPase Biosensors. *Methods Mol. Biol.* *1821*, 71–85. https://doi.org/10.1007/978-1-4939-8612-5_6.
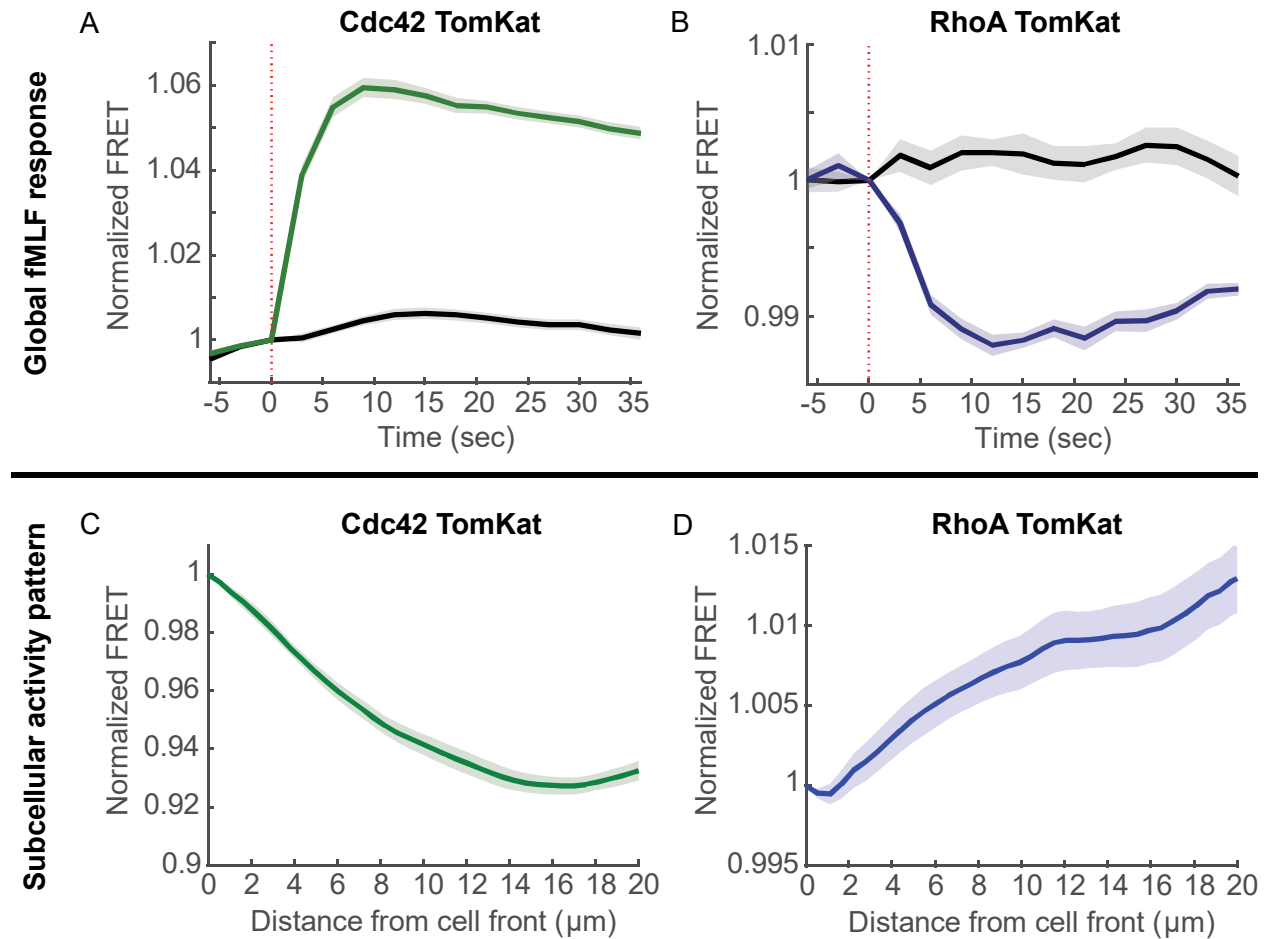
4.8 Figures

Figure 4.1. Characterization of Cdc42 and RhoA TomKat sensors

(A) Response of the Cdc42 FRET biosensor to fMLF stimulation. fMLF was added at 0 seconds, indicated by the dashed vertical line. The response of control cells, which were treated with media without fMLF, is shown in black. (B) Response of the RhoA FRET biosensor to fMLF stimulation. fMLF was added at 0 seconds, indicated by the dashed vertical line. The response of control cells, which were treated with media without fMLF, is shown in black. (C) The subcellular activity pattern of Cdc42 reported by the Cdc42 TomKat sensor. FRET ratio on the Y-axis is shown as a function of distance from the cell front on the X-

axis. (D) The subcellular activity pattern of RhoA reported by the RhoA TomKat sensor. FRET ratio on the

Y-axis is shown as a function of distance from the cell front on the X-axis.
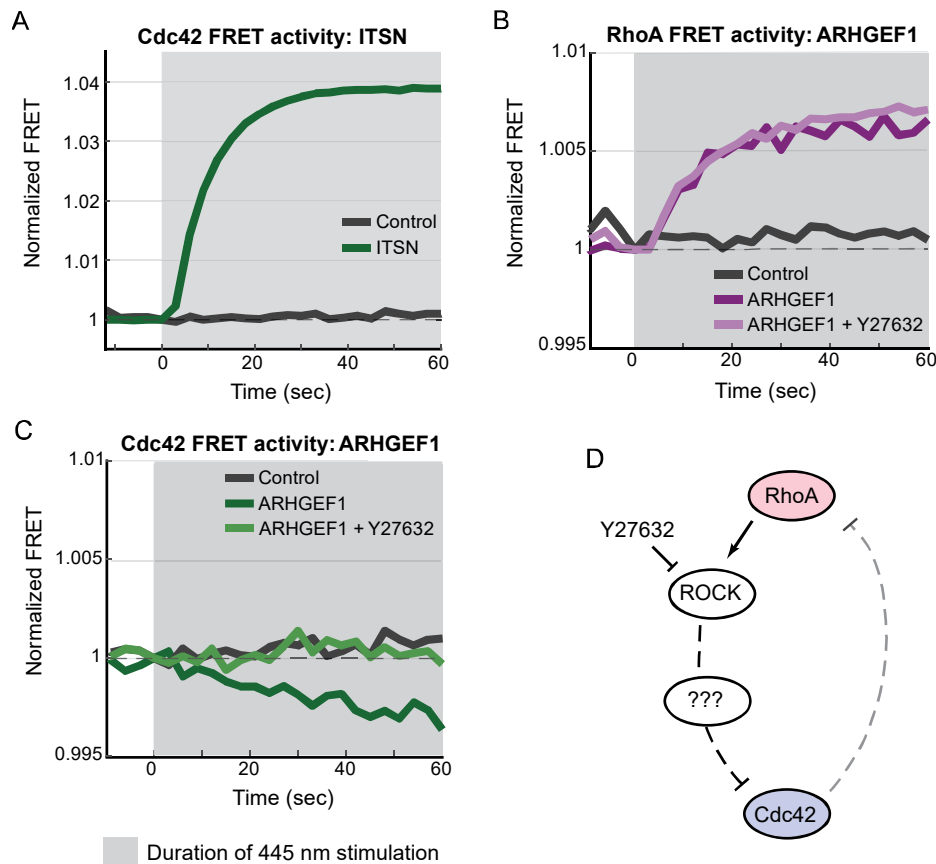
Figure 4.2. Rho GTPase signaling crosstalk revealed through global optogenetic stimulation

(A) Response of the Cdc42 TomKat sensor to global optogenetic activation of Cdc42. The gray shading indicates the time of 445 nm light stimulation. The response of control cells expressing the mCitrine-SspB construct without the ITSN domain is shown in black. (B) Response of the RhoA TomKat sensor to global optogenetic activation of RhoA. The gray shading indicates the time of 445 nm light stimulation. The response of untreated cells is shown in dark magenta. The response of cells treated with ROCK inhibitor (Y27632) is shown in light magenta. The response of control cells expressing the mCitrine-SspB construct without the ARHGEF1 domain is shown in black. (C) Response of the Cdc42 TomKat sensor to global optogenetic activation of RhoA. The response of untreated cells is shown in dark green. The response of cells treated with ROCK inhibitor (Y27632) is shown in light green. The response of control cells expressing the mCitrine-SspB construct without the ITSN domain is shown in black. (D) An illustration of the molecular circuit mediating mutual RhoA-Cdc42 crosstalk. RhoA signals through ROCK to inhibit

Cdc42 activity. Y27632 blocks this inhibition. The downstream players of this pathway, including potential

Cdc42 GAPs, remain unknown. Cdc42 has also been shown to mutually antagonize RhoA activity.
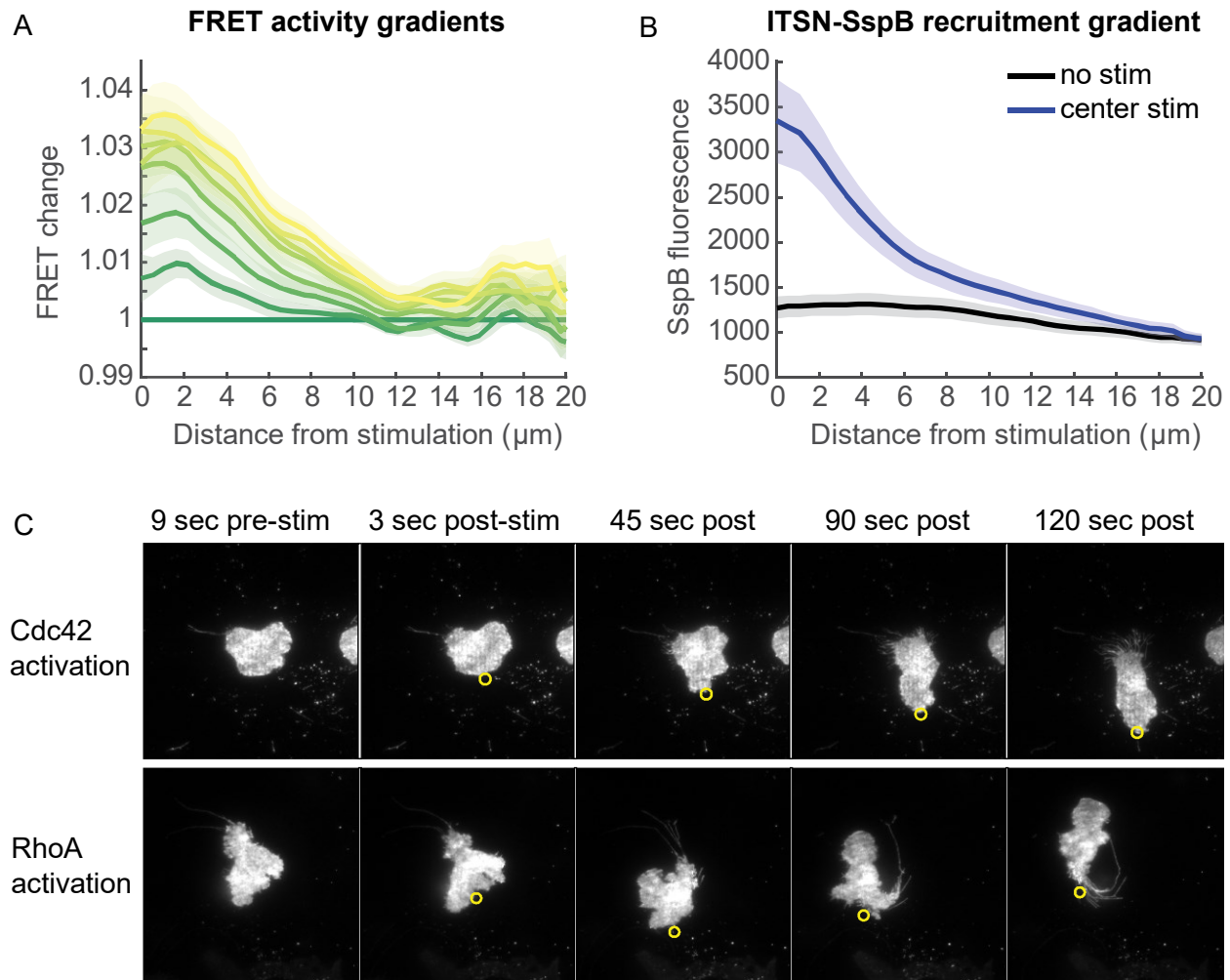
Figure 4.3. Subcellular optogenetic Rho GTPase activation is sufficient to drive cell migration

(A) Change in Cdc42 FRET activity in response to optogenetic Cdc42 activation at the cell center. FRET

change on the Y-axis is depicted as a function of distance from the stimulation site on the X-axis. FRET

values are normalized to the frame 3 seconds before optogenetic stimulation began. FRET activity gradients

at early time points are shown in green and FRET activity gradients at later time points are shown in yellow.

(B) The recruitment gradient of the ITSN-mCitrine-SspB construct captured after the final imaging time

point is shown in blue, while the gradient of unstimulated cells is shown in black. Recruitment is depicted

by ITSN-mCitrine-SspB fluorescence intensity on the Y-axis as a function of distance from the stimulation

site on the X-axis. (C) Top panel: Cell migratory behavior in response to local Cdc42 activation at the cell

edge. The first panel shows the cell prior to optogenetic activation. The second through fifth panels show

the cell's movement in response to Cdc42 activation in the region indicated by the yellow cursor at 3, 45, 90, and 120 seconds post-stimulation. Bottom panel: Cell migratory behavior in response to local RhoA activation at the cell edge. The first panel shows the cell prior to optogenetic activation. The second through fifth panels show the cell's movement in response to RhoA activation in the region indicated by the yellow cursor at 3, 45, 90, and 120 seconds post-stimulation.

Chapter 5

Discussion and concluding remarks

Dean E. Natwick[1]

[1]Department of Microbiology and Molecular Genetics, University of California, Davis, Davis, CA 95616,

United States

5.1 Preface

This chapter provides an overview of the work presented in this dissertation, places it within the context

of the current research in the field, and presents opinions on important future directions of investigation.

5.2 Discussion and concluding remarks

Neutrophils, like many cell types, are "quick thinkers" and "multi-taskers". In other words, they are designed to take in environmental information, process it on second timescales, and enact decisive responses. It is becoming increasingly clear that Rho GTPase signaling networks are a core part of this cellular logic in many contexts. There is also mounting appreciation for the true complexity of these signaling processes- they are highly dynamic, have precise spatial organizations, and are context dependent, even within cell types[1]. Regulation by specialized sets of GEFs and GAPs allows Rho GTPases to respond to different stimuli, and complex wiring, including feedback and crosstalk connections, allows fine tuning of response dynamics[2]. Therefore, dissecting the architecture of the Rho GTPase signaling pathways that control different cell behaviors requires highly sophisticated tools and approaches that can be utilized in diverse cell models.

The photo-uncaging under agarose assay described in Chapter 2 is especially useful for understanding how receptor-driven signals impinge on GTPase activities. Indeed, this approach was used to understand the spatial organization and dynamics of Rac, Cdc42, RhoA, and Ras in neutrophils chemotaxing in fMLF gradients[3]. It was shown that symmetry-breaking of Cdc42 activity at the cell front is predictive of cell turning, implicating Cdc42 as a central protein for steering during chemotaxis. Cdc42 activity also predicted polarity orientation when morphologically unpolarized cells were stimulated with uniform fMLF. These results are in line with Cdc42's conserved role as a major regulator of polarity[4–6]. The photo-uncaging under agarose assay was also used as part of a genetic screen for regulators of chemotaxis in PLB-985 cells[7]. This work identified both known and novel components involved in chemotaxis and assigned specialized roles to many of them. Notably, knockdown of the $G_i\alpha$ subunit resulted in strong directionality defects. Taken together, these two studies place $G_i\alpha$ and Cdc42 in pathways that integrate directional sensing with polarity and illustrate the power of these approaches in disentangling chemotaxis signaling.

For studying the inherent wiring of Rho GTPase networks, such as autonomous feedback and crosstalk connections, the ability to precisely perturb Rho GTPase activities and measure responses is essential. The work presented in Chapters 3 and 4 of this dissertation lays the groundwork for such experiments. Past work in fibroblasts found evidence for hierarchical crosstalk from Cdc42 to Rac, then from Rac to RhoA[8,9]. Whether a similar hierarchy underlies Rho GTPase wiring in neutrophils has remained unclear for many years. Given the role of Cdc42 in cell steering described above, crosstalk wiring that enables Cdc42 to guide Rac, RhoA, and Ras activities seems plausible. However, the RhoA-to-Cdc42 crosstalk identified in undifferentiated PLB-985 cells in Chapter 4 of this work suggests that signaling connections between Rho GTPases in neutrophils may be more complex.

The RhoA to Cdc42 crosstalk pattern revealed in this work aligns with our emerging understanding of the relationship between cell front and rear domains in neutrophils. Throughout the 2000s, the Henry Bourne's lab at UCSF characterized mutual antagonism between these regions of the cell[10]. Notably, over-expression of a constitutively-active form of RhoA inhibited the formation of a strong front domain in HL-60 cells[10]. While their work focused primarily on antagonistic crosstalk between Rac and RhoA, antagonism between Cdc42 and RhoA also fits with much of the existing data. Additionally, recent work in PLB-985 cells used an optogenetic GPCR to reveal an inhibitory role for the RhoA/ROCK/myosin pathway in allowing repolarization and establishment of a cell front[11]. The results from Chapter 4 corroborate these findings and suggest that this inhibitory behavior may function independent of receptor activity. There are also multiple lines of evidence suggesting that the cell front has a similar role in limiting cell rear activity, and that the cell front may even help to pattern the cell rear through long range positive crosstalk[10,12,13]. The tools described in this work offer the opportunity to fully explore past findings, measure the spatial component of crosstalk connections, and ultimately develop a complete map of Rho GTPase crosstalk in neutrophils.

Looking further into the future, understanding how different features of Rho GTPase networks are controlled through GEF and GAP regulation will be a major challenge. This will be especially difficult given the complex nature of GEF and GAP proteins and the dependence of cell and

environmental context on regulatory mechanisms[14]. An important advancement on this front was recently made with the development of GEF activity biosensors[15,16]. These FRET-based sensors take advantage of a conserved structural change among many Dbl family GEFs to record protein activity in live cells, and functional sensors for several GEFs were presented. Importantly, specialization within the regulatory network was clearly identified, as distinct spatial and temporal patterns of activity were seen across different GEFs. In this work, statistical analysis was used to infer causation between GEF activity, downstream Rho GTPase activity, and changes in cell edge velocity. While this has begun to add a new layer to our understanding of Rho GTPase regulation, additional complementary approaches are needed. For instance, functional roles must be determined for the vast majority of GEFs that remain uncharacterized[1]. To this end, developing high-throughput functional assays and systematic genetic screens in neutrophils will be important. Furthermore, negative regulation of GTPases by GAPs remains an especially neglected area of study. Negative regulation is vital in balancing and focusing positive signaling events in space and time[17]. Therefore, our understanding of Rho GTPase signal processing will depend on a much deeper exploration of the roles of GAPs and other potential negative regulators.

Diverse mechanisms of regulation even further upstream of GEFs and GAPs are invariably important in tuning signaling events as well[18]. Better understanding these mechanisms within chemotaxis pathways will be an ultimate goal for the field. Eventually, our understanding of Rho GTPase networks, their GEF and GAP regulation, and regulatory steps even further upstream, may start to converge with our growing knowledge of early signaling events driven by receptors and associated G-proteins. At that point, we may finally start building a holistic view of the molecular events that underlie the regulation of complex cell behaviors like chemotaxis.

5.3 References

(1)   Goedhart, J., van Unen, J. (2019) Molecular Perturbation Strategies to Examine Spatiotemporal

Features of Rho GEF and Rho GTPase Activity in Living Cells. *Small GTPases 10* (3), 178–186.

https://doi.org/10.1080/21541248.2017.1302551.

(2)   Müller, P. M., Rademacher, J., Bagshaw, R. D., Wortmann, C., Barth, C., Unen, J. Van, Alp, K.

M., Giudice, G., Eccles, R. L., Heinrich, L. E., Pascual-vargas, P., Sanchez-castro, M.,

Brandenburg, L., Mbamalu, G., Tucholska, M., Spatt, L., Czajkowski, M. T., Welke, R., Zhang,

S., Nguyen, V., Rrustemi, T., Trnka, P., Freitag, K., Larsen, B., Popp, O., Mertins, P., Gingras, A.,

Roth, F. P., Colwill, K., Bakal, C., Pertz, O., Pawson, T., Petsalaki, E., Rocks, O. (2020) Systems

Analysis of RhoGEF and RhoGAP Regulatory Proteins Reveals Spatially Organized RAC1

Signalling from Integrin Adhesions. *Nat. Cell Biol. 22* (April), 498–511.

https://doi.org/10.1038/s41556-020-0488-x.

(3)   Yang, H. W., Collins, S. R., Meyer, T. (2016) Locally Excitable Cdc42 Signals Steer Cells during

Chemotaxis. *Nat. Cell Biol. 18* (2), 191–201. https://doi.org/10.1038/ncb3292.

(4)   Adams, A. E. M., Johnson, D. I., Longnecker, R. M., Sloat, B. F., Pringle, J. R. (1990) CDC42 and

CDC43, Two Additional Genes Involved in Budding and the Establishment of Cell Polarity in the

Yeast Saccharomyces Cerevisiae. *J. Cell Biol. 111* (July), 131–142.

(5)   Kay, A. J., Hunter, C. P. (2001) CDC-42 Regulates PAR Protein Localization and Function to

Control Cellular and Embryonic Polarity in C . Elegans. *Curr. Biol. 42*, 474–481.

(6)   Wu, X., Li, S., Chrostek-grashoff, A., Czuchra, A., Meyer, H., Yurchenco, P. D., Brakebusch, C.

(2007) Cdc42 Is Crucial for the Establishment of Epithelial Polarity During Early Mammalian

Development. *Dev. Dyn.* No. 236, 2767–2778. https://doi.org/10.1002/dvdy.21309.

(7)   Collins, S. R., Yang, H. W., Bonger, K. M., Guignet, E. G., Wandless, T. J., Meyer, T. (2015)

Using Light to Shape Chemical Gradients for Parallel and Automated Analysis of Chemotaxis.

Mol. Syst. Biol. 11 (4), 804. https://doi.org/10.15252/msb.20156027.

(8)   Ridley, A. J., Paterson, H. F., Johnston, C. L., Diekmann, D., Hall, A. (1992) The Small GTP-

        Binding Protein Rac Regulates Growth Factor-Induced Membrane Ruffling. *Cell 70* (3), 401–410.

        https://doi.org/10.1016/0092-8674(92)90164-8.

(9)   Nobes, C. D., Hall, A. (1995) Rho, Rac, and Cdc42 GTPases Regulate the Assembly of

        Multimolecular Focal Complexes Associated with Actin Stress Fibers, Lamellipodia, and

        Filopodia. *Cell 81* (1), 53–62. https://doi.org/10.1016/0092-8674(95)90370-4.

(10)   Xu, J., Wang, F., Van Keymeulen, A., Herzmark, P., Straight, A., Kelly, K., Takuwa, Y.,

        Sugimoto, N., Mitchison, T., Bourne, H. R. (2003) Divergent Signals and Cytoskeletal Assemblies

        Regulate Self-Organizing Polarity in Neutrophils. *Cell 114* (2), 201–214.

        https://doi.org/10.1016/S0092-8674(03)00555-5.

(11)   Hadjitheodorou, A., Bell, G. R. R., Ellett, F., Shastry, S., Irimia, D. (2021) Directional

        Reorientation of Migrating Neutrophils Is Limited by Suppression of Receptor Input Signaling at

        the Cell Rear through Myosin II Activity. *bioRxiv* 1–57.

(12)   Weiner, O. D., Rentel, M. C., Ott, A., Brown, G. E., Jedrychowski, M., Yaffe, M. B., Gygi, S. P.,

        Cantley, L. C., Bourne, H. R., Kirschner, M. W. (2006) Hem-1 Complexes Are Essential for Rac

        Activation , Actin Polymerization , and Myosin Regulation during Neutrophil Chemotaxis. *PLoS

        Biol. 4* (2), 186–199. https://doi.org/10.1371/journal.pbio.0040038.

(13)   O'Neill, P. R., Kalyanaraman, V., Gautam, N. (2016) Subcellular Optogenetic Activation of

        Cdc42 Controls Local and Distal Signaling to Drive Immune Cell Migration. *Mol. Biol. Cell 27*

        (9), 1442–1450. https://doi.org/10.1091/mbc.E15-12-0832.

(14)   Cherfils, J., Zeghouf, M. (2012) Regulation of Small GTPases by GEFs, GAPs, and GDIs.

        Physiol. Rev. No. 93, 269–309. https://doi.org/10.1152/physrev.00003.2012.

(15)   Marston, D. J., Vilela, M., Huh, J., Ren, J., Azoitei, M. L., Glekas, G., Danuser, G., Sondek, J.,

        Hahn, K. M. (2020) Multiplexed GTPase and GEF Biosensor Imaging Enables Network

        Connectivity Analysis. *Nat. Chem. Biol. 16*, 826–833. https://doi.org/10.1038/s41589-020-0542-9.

(16)   Natwick, D. E., Collins, S. R. (2020) Decoding GEFs of Animated Cells. *Nat. Chem. Biol. 16* (8),

812–813. https://doi.org/10.1038/s41589-020-0570-5.

(17)   Bell, G. R. R., Rincón, E., Akdoğan, E., Collins, S. R. (2021) Optogenetic Control of Receptors

Reveals Distinct Roles for Actin- and Cdc42-Dependent Negative Signals in Chemotactic Signal

Processing. *bioRxiv* 1–43.

(18)   Hodge, R. G., Ridley, A. J. (2016) Regulating Rho GTPases and Their Regulators. *Nat. Rev. Mol.*

Cell Biol. 17 (8), 496–510. https://doi.org/10.1038/nrm.2016.67.